The impact of Radial and Non-Radial IMF on the Earth's Magnetopause Size and Shape, and Dawn-Dusk Asymmetry from Global 3D Kinetic Simulations

Suleiman M Baraka [1,3], O. Le Contel [2], L. Ben−Jaffel[3], W. B. Moore[1,4]

[1]National Institute of Aerospace, 100 Exploration Way, Hampton, VA 23666
[2]Laboratoire de Physique des Plasmas, UMR7648 ,CNRS/Sorbonne Université/Université Paris-Saclay/Observatoire de Paris/Ecole Polytechnique Institut Polytechnique de Paris, Palaiseau, France.
[3]Institut d'Astrophysique de Paris, UMR7095, Sorbonne Université, Paris, France
[4]Hampton University, 154 William R. Harvey Way Hampton, VA 23668

Key Points:

- Magnetosphere.
- IMF Radial and Quasi Radial Orientations.
- Solar Wind.
- Temperature anisotropy and velocity distribution function.
- IAPIC Kinetic Electromagnetic Relativistic Particle Code.

Corresponding author: Suleiman M Baraka, `suleiman.baraka@nianet.org`

Abstract

The boundary between the solar wind (SW) and the Earth's magnetosphere, the magnetopause (MP), is highly dynamic. Its location and shape depend on SW dynamic pressure and interplanetary magnetic field (IMF) orientation. We use a 3D kinetic Particle-In-Cell code (IAPIC) to simulate an event observed by THEMIS spacecraft on July 16, 2007. We investigate the impact of radial (θ_{Bx}=0°) and non-radial (θ_{Bx}=50°) IMF on the shape and size of Earth's MP for a dipole tilt of 31° using maximum density gradient and pressure balance methods. Using the Shue model as a reference (MP at 10.3 R_E), we find that for quasi-radial IMF the MP expands by 1.4 and 1.7R_E along the sun-Earth (OX) and tilted magnetic (Tilt) axes, respectively, and it expands by 0.5 and 1.6R_E for radial IMF along the same respective axes. When the effect of backstreaming ions is removed from the bulk flow, the expansion ranges are 1.0 and 1.3R_E and 0.2, an 1.2R_E respectively. It is found that the percentage of backstreaming to bulk flow ions are 16.5%, and 20% for radial and non-radial IMF. We also show that when the backstreaming ions are not resolved, up to 40% of the observed expansion that is due to backstreaming particles can be inadvertently attributed to a change in the SW upstream properties. Finally, we quantified the temperature anisotropy in the magnetosheath, and observe a strong dawn-dusk asymmetry in the MP location.

Plain Language Summary

The Earth's magnetopause (MP) is a sensitive region where the pressure of the Earth magnetic field balances the shocked solar wind ram and thermal pressures. Accurate space weather monitoring and forecast require an in-depth knowledge of this region and of the physical processes that affect it. We investigate effects of the orientation of the interplanetary magnetic field (IMF) on the MP size, location, and shape by using a numerical technique (3D kinetic simulation) that explicitly resolves ion and electron motion. We are able to extract the shape and location of the MP in three dimensions to estimate the sensitivity of the MP position to the ambient IMF and solar wind conditions, while our explicit tracking of ion motions allows us to investigate the role of ion species backscattered by the

Earth's bow shock and magnetosheath. We find that when the IMF has a strong component in the Earth-Sun direction (radial or quasi-radial IMF), these backscattered ions play an important role in reducing the effective pressure of the incoming solar wind and allowing the MP to expand outward.

1 Introduction

The magnetic fields of planets such as Mercury, Earth, and the giant planets present an obstacle to the supersonic solar wind (SW). As a result, a shock forms and the solar wind is redirected around the obstacle producing a cavity which is called the magnetosphere (e.g., Parks, 1991). The boundary between the solar wind and the plasma in the magnetosphere is the magnetopause (MP). At the subsolar point, the classical fluid description of the solar wind stagnation flow derives the location of the magnetopause by the balance between the planetary magnetic field pressure and the dynamic pressure of the SW. Plasma boundary layers form on either side of the magnetopause with the magnetosheath boundary layer (MSBL) on the sunward side and the low-latitude boundary layer (LLBL) on the magnetosphere side. Both layers play an important role in plasma exchange across the magnetopause (e.g., Pi et al., 2018).

The magnetopause structure is significantly influenced by the interplanetary magnetic field (IMF) orientation. While the impact of southward (Yu & Ridley, 2009; Heikkila, 2011; Tan et al., 2011; Suvorova & Dmitriev, 2015; Berchem et al., 2016) and northward IMF (Sorathia et al., 2019; Luo et al., 2013; Bobra et al., 2004; Wang et al., 2018) on the dynamics of Earth's magnetosphere have been extensively studied in the last four decades, only recently has attention been focused on radially-dominant IMF conditions, which will be called radial IMF for the remainder of this paper. For most solar wind plasma conditions at the orbital position of planets, bow shocks are collisionless and supercritical shocks, which by definition, reflect and accelerate a fraction of the plasma impinging on them. These backstreaming particles lead to the formation of the ion foreshock region upstream (e.g., Turner et al., 2018, p. 206).

Following early satellite observations (Greenstadt et al., 1968; Asbridge et al., 1968), the idea of an extended foreshock that diverts the solar wind around the magnetosphere and reduces the solar wind dynamic pressure at the subsolar magnetopause was proposed for radial IMF conditions (Fairfield et al., 1990; Merka et al., 2003; Jelínek et al., 2010;

Suvorova et al., 2010). The distance and shape of the equatorial magnetopause is strongly affected by radial IMF, resulting in a global expansion of the magnetopause (Grygorov et al., 2017). (Zhang et al., 2019) found that a dawn-dusk asymmetry exists in the magnetosheath, directly related to the IMF orientation. Evidently, the plasma distribution and the IMF are correlated to these asymmetries which are either generated at the bow shock or inside the magnetosheath itself.

Most magnetopause observations during radial IMF have noted a large magnetopause expansion that was connected with a significant distortion of the magnetopause surface. Large magnetopause distortion and anomalous sunward magnetosheath flows were reported in one radial IMF event by (Shue et al., 2009). The finding of magnetopause displacement during radial IMF conditions was also documented in a statistical study based on a large set of magnetopause crossings using THEMIS (Dušík et al., 2010) and GOES (Park et al., 2016). A systematic increase of observed magnetopause distances for radial IMF was found, ranging from $0.3R_E$ at 90° cone angle to $\approx 1.7R_E$ at 0° or 180° cone angles compared to empirical models. In contrast, using THEMIS data and empirical models of the MP, Grygorov et al. (2017) concluded that the distance of the equatorial magnetopause is strongly affected by radial IMF, expanding globally and independent of the local time, upstream value of other solar wind parameters or the tilt of the Earth magnetic dipole.

It is interesting to remark that no self-consistent model exists today in the literature that can explain the observed MP displacement or its asymmetry, particularly with the difficulty MHD approaches have to accurately model reflected SW ions in the foreshock region (Sibeck et al., 2001). In a recent study, (Samsonov et al., 2017) used previous statistical results to suggest that the density and velocity in the foreshock region decrease to $\sim$ 60% and $\sim$94% of the undisturbed SW values when the cone angle falls below 50° causing a drop in the SW dynamic pressure of $\sim$ 53% that might cause the MP displacement. In a second step, those authors modified the upstream SW parameters in a global MHD model to take these foreshock effects into account, which helped them predict MP distances during non-radial

IMF intervals close to those observed by THEMIS. More precisely, using time dependent SW conditions provided by ACE and WIND measurements in their simulations, they applied a $\sim 53\%$ dynamic pressure reduction as soon as the SW cone angle becomes smaller than 50°. This limit was chosen in order to smooth the swap between radial (reduced dynamic pressure) and non-radial (unchanged dynamic pressure) regimes (Samsonov et al., 2017). In the present study, we employ constant upstream SW conditions. For the sake of covering the full range of cone angles considered in the simulations of (Samsonov et al., 2017), we have performed simulations for the two limit cases of 0° (referred to as radial IMF) and $\sim 50^\circ$ cone angle (referred to as non-radial IMF). We note that there is no consistent usage in the literature of the terms radial or quasi-radial IMF.

According to (Samsonov et al., 2017), the strong total pressure decrease in the data seems to be a local, rather than a global, phenomenon. Those authors conceded that their model was not self-consistent in the sense that the modified upstream SW parameter adjustment was global and not specific to the foreshock region for which the statistical results (discussed above) were initially derived. One of the goals of this study is to investigate the role of backscattered ions in producing decreased SW pressure at the bowshock by resolving them in a 3D kinetic simulation.

In addition to the expansion of the MP, the other focus of this study is the generation of dawn-dusk asymmetry under radial IMF, which has been investigated for many decades (Akasofu et al., 1982; Akasofu, 1991; Haaland et al., 2017, and references therein). Dawn-dusk asymmetries are ubiquitous features of the coupled solar wind-magnetosphere-Ionosphere system. During the last decades, increasing availability of satellite and ground-based measurements has made it possible to study these phenomena in more detail (e.g., B. M. Walsh, 2017). Most studies reported so far agree that the dawn-dusk asymmetry is primarily the result of the Parker spiral solar wind impinging with a specific geometric configuration that impacts and preconditions the magnetosphere (e.g., Haaland et al., 2017, and references therein). Under radial IMF conditions, one would then expect the Parker

spiral effect to disappear while other physical processes, like kinetic effects, would drive any dawn-dusk asymmetry. For instance, statistical studies based on THEMIS and Cluster measurements confirm a rather global expansion of the magnetopause under radial IMF without significant dawn-dusk asymmetries detected (Zhang et al., 2019). The same statistical study showed that magnetic reconnection (MR) is nearly absent during radial IMF, in contrast to the north IMF conditions during which MR and the consequent dawn-dusk asymmetries are strong (Zhang et al., 2019).

Kinetic effects are expected to trigger a large set of distinct dawn-dusk asymmetries upstream of the magnetosphere due to the formation of the foreshock region that is connected with solar wind particles backscattered at the bow shock. Although much of the plasma passes through the bow shock, the reflected population generates a number of plasma instabilities, which trigger waves and generate wave-particle interactions as well as other dynamics at the non-parallel shock that should favor dawn-dusk asymmetries (e.g., B. M. Walsh, 2017, and references therein). The radial IMF condition would thus be the ideal configuration to reveal such kinetic effects and and determine their role in producing the dawn-dusk asymmetry so far observed (Zhang et al., 2019). For reference, using Cluster single/multiple spacecraft measurements, Haaland et al. (2014) discussed the dawn-dusk asymmetry at the flanks and at the dayside MP. Similar results were also reported by Haaland et al. (2019), as observed by two of the THEMIS spacecraft, showing the magnetopause being thicker on dawn ($\sim 14\lambda_i$, λ_i being the ion inertial length) than on dusk ($\sim 8\lambda_i$), however no radial IMF conditions were included in the statistical study. Additionally, other observations from INTERBALL-1 and MAGION-4 spacecraft revealed asymmetry and deformation at the turbulent magnetopause (Šafránková et al., 2000). Using Geotail observations for northern and southern IMF, Wang et al. (2006) thoroughly discussed the dawn-dusk asymmetry in ion density and temperature based on equatorial distribution of plasma sheet ions.

To interpret the magnetopause motion and the dawn-dusk asymmetry, many sophisticated models have been utilized, ranging from MHD to hybrid simulations. Early theoretical studies showed a contrast of 10%-20% between dawn and dusk bulk plasma properties (e.g., Němeček et al., 2002; B. M. Walsh et al., 2012), however, those MHD-based models do not explicitly resolve kinetic effects, particularly at the foreshock region. For instance, using a global hybrid model (kinetic ions and fluid electrons), Blanco-Cano et al. (2009) studied radial IMF ($\theta_{vB} = 0$) impact on the solar wind interaction with the Earth's magnetosphere. The study focused on the micro-physics processes and wave-particle interactions in the foreshock region but briefly mentioned the dawn-dusk asymmetry issue. Three other models i.e. hybrid, Hall-less and Hall-MHD simulations have been tested in one study by Karimabadi et al. (2004) for the analysis of MR regimes with the conclusion that dawn-dusk asymmetry is obtained and should be related to ions flow. Recently, Turc et al. (2020) used the hybrid -Vlasiator 2D-3V code to study asymmetries in the Earth magnetosheath for different IMF conditions. For reference, the Vlasiator code provides a kinetic description of ions, solving directly the Vlasov equation for the particle distribution function in 2D-3D space, but assumes a fluid description for electrons (e.g. Palmroth et al., 2018). The authors report asymmetries larger than observed for the magnetic field strength, the plasma density, and bulk velocity, a discrepancy that was attributed to using a single set of upstream conditions in their simulations. It is interesting to remark that those authors obtained a stronger asymmetry for magnetic field strength when IMF gets closer to the radial configuration. However, it was not clear how the 2D spatial assumption and the fluid description of electrons in their simulations affected the reported magnetosheath asymmetries.

Based on the discussion above, two important questions appear: 1) what happens to the magnetopause shape, size, and location if flow-aligned IMF is applied to the system when kinetic effects are included for all species? and 2) does this generate asymmetry in the dawn-dusk and south-north directionsSo in the dayside magnetosphere?

To answer these questions, we undertake a modeling study utilizing IAPIC, a particles-in-cell code (discussed in section 2). Our strategy is to be able to follow ions and electrons self-consistently with the Maxwell equations describing the fields. Thus the full range of collisionless plasma physics is captured for the macro-ions and macro-electrons involved in IAPIC, yet with limitations due to the grid spatial resolution and assumptions made on the plasma properties (particles density, ion/electron mass ratio, etc.) that we carefully discuss in section 2 (see Blanco-Cano et al., 2006; Eastwood, 2008; Jacobsen et al., 2009; Brackbill, 2011; Masters et al., 2013; Ben-Jaffel & Ballester, 2014; S. Baraka, 2016). We adopt the initial and the boundary conditions reported in (Suvorova et al., 2010; Samsonov et al., 2017), we used single physical units for each parameters that were used in CCMC reported in (Samsonov et al., 2017).

This paper is structured as follows. This section has introduced the impact of radial IMF orientation on the dynamics of the Earth's magnetosphere and presented a brief survey of observations of asymmetry in planetary magnetospheres. Two IMF orientations, namely, radial IMF ($B = B_x$) and non-radial IMF (B_x & $B_y > B_z$) will be covered in the current study.

In section 2, we describe the IAPIC code in details. The scaling of plasma parameters is also presented and tabulated.

In section 3,we show our findings regarding the magnetopause motion and the magnetosheath asymmetry, an opportunity to compare to previous modeling results and observations. In section 4, we discuss in details about the impact of the purely and non-radial IMF on the dynamics of the Earth's magnetosphere, in light of the results obtained so far. In section 5, we present a summary of our findings and future related work.

2 Initial conditions and Simulation Model: IAPIC

2.1 Simulation Model: IAPIC

We use the Institut d'Astrophysique de Paris-Particle-In-Cell EM 3D global code (IAPIC) for treating the plasma kinetically. IAPIC has previously been applied to simulate various magnetospheres in the solar system (S. Baraka & Ben-Jaffel, 2011; Ben-Jaffel & Ballester, 2013, 2014; S. Baraka, 2016). IAPIC handles the equations of motion for large number of macro-particles (macro-ions and macro-electrons) self-consistently under the direct impact of electromagnetic fields through Lorentz force law (S. Baraka & Ben-Jaffel, 2007; Artemyev & Zelenyi, 2012).

The code was originally written by (Buneman et al., 1992) which used the boundary conditions reported in (Lindman, 1975) and charge conserving conditions as described in (Villasenor & Buneman, 1992). we use physical units for each parameter from (Samsonov et al., 2017) and scaled them to IAPIC values using a transformation matrix to convert GSM coordinates to the IAPIC code coordinates (see Fig. 1) as reported in (Cai et al., 2003). The solar wind parameters are normalized to spatial and temporal parameters and tabulated in Table 1 for radial IMF and Table2 for non radial IMF (see also, Table 1, Cai et al., 2015).

We follow the evolution of the fields and particles within a 61x45x45 R_E domain with Earth centered and 20 R_E downstream of the sunward (inlet) side (Table 1). We chose time step $\Delta t = 3700$ as our comparison point which corresponds to 24 minutes of real time (approximately twice the SW transit time) after starting the simulation. Each time step is equivalent to ≈ 0.38 sec and the spatial resolution of the code is $0.2R_E$. We track 7.0×10^7 particle pairs, with an ion to electron mass ratio of 64.

Our normalized solar wind parameters to temporal and spatial values for both IMF orientations are given in Tables 1 and 2 for radial and non-radial IMF, respectively. The parameters are set such that a consistent initial conditions are validated before the code run

starts, denoted as $\Delta t = 0$, and at the step time, where the current study is considered i.e. $\Delta t = 3700$. These two tables are compared to similar study by (Cai et al., 2015)

Step time		Δt =0		Δt =3700	
Species/Parameters	Normalization	ions	electrons	ions	electrons
Thermal velocity, $V_{thi,e}$	$\tilde{v}_{thi,e} = \frac{v_{thi,e}}{\Delta/\Delta t}$	0.177	0.708	0.135	1.069
Debye length, $\Delta_{i,e}$	$\tilde{\lambda_{i,e}} = \frac{\tilde{v_{thi,e}}}{\tilde{\omega_{pi,e}}}$	0.8	0.4	0.52	0.52
Larmor radius, $\lambda_{i,e}$	$\tilde{\rho}_{ci,e} = \frac{\tilde{v}_{thi,e}}{\tilde{\omega}_{ci,e}}$	8.85	0.49	45	2.6
Gyro-frequency $\omega_{ci,e}$	$\tilde{\omega}_{ci,e} = \omega_{ci,e} \cdot \Delta t$	0.02	1.425	0.003	0.41
Plasma-frequency $\omega_{pi,e}$	$\tilde{\omega}_{pi,e} = \omega_{pi,e} \cdot \Delta t$	0.22	1.77	0.27	2.14
Temperature, $T_{i,e}$	$\tilde{T_e} = 2\tilde{v}_{the}^2$, $\tilde{T_i} = 2\tilde{v}_{thi}^2 \frac{m_i}{m_e}$	4.	1.	2.33	2.28
Gyroperiod	$\tilde{\tau}_{ci,e} = \frac{2\pi}{\tilde{\omega}_{ci,e}}$	314.15	4.4	2094.34	15.32
Inertial length $d_{i,e}$	$\tilde{d_{i,e}} = \frac{\tilde{c}}{\tilde{\omega_{pi,e}}}$	2.27	2.82	1.89	0.23

Unitless values

Step time	Δt =0	Δt =3700
Sound speed C_s	0.045	0.050
Alfvén speed v_A	0.050	0.012
Alfvén Mach number M_A	2.83	5.4351
Sonic Mach number M_s	3.16	1.3
Magnetosonic Mach number M_{ms}	2.0	1.27

Loaded Simulation Box Information

grid size		$\Delta = 0.2R_E = \Delta x = \Delta y = \Delta z$
Time Step		$\Delta t = \Delta_x/\Delta_v = 7.08$
Simulation box size		$(305 \times 225 \times 255)\Delta$
# of pair-particles		7×10^7 ion/electrons pairs
Ion to electron mass ratio		64
Particle density		$n_i = n_e$=$4/\Delta^3$

Table 1. Normalized solar wind parameters at the initial state and after 3700 Δt in the solar wind for both ions and electrons for radial IMF.

Step time		Δt =0		Δt =3700	
Species/Parameters	Normalization	ions	electrons	ions	electrons
Thermal velocity, $V_{thi,e}$	$\tilde{v}_{thi,e} = \frac{v_{i,e}}{\Delta/\Delta t}$	0.177	0.708	0.127	1.027
Debye length, $\lambda_{Di,e}$	$\tilde{\lambda_{i,e}} = \frac{v_{t\tilde{h}i,e}}{\tilde{\omega_{pi,e}}}$	0.8	0.4	0.529	0.52
Larmor radius, $\lambda_{i,e}$	$\tilde{\rho}_{ci,e} = \frac{\tilde{v}_{thi,e}}{\tilde{\omega}_{ci,e}}$	3.175	0.29	25.4	1.95
Gyro-frequency $\omega_{ci,e}$	$\tilde{\omega}_{ci,e} = \omega_{ci,e} \cdot \Delta t$	0.04	2.435	0.005	0.525
Plasma-frequency $\omega_{pi,e}$	$\tilde{\omega}_{pi,e} = \omega_{pi,e} \cdot \Delta t$	0.22	1.77	0.24	1.955
Temperature, $T_{i,e}$	$\tilde{T}_e = 2\tilde{v}^2_{the}$, $\tilde{T}_i = 2\tilde{v}^2_{thi}\frac{m_i}{m_e}$	4.010	1.0	2.065	2.109
Gyroperiod	$\tilde{\tau}_{ci,e} = \frac{2\pi}{\tilde{\omega}_{ci,e}}$	157.27	2.58	1256.63	11.960
Inertial length $d_{i,e}$	$\tilde{d_{i,e}} = \frac{\tilde{c}}{\tilde{\omega_{pi,e}}}$	2.27	0.282	2.08	0.255

`Unitless values`

Step time	1	3700
Sound speed C_s	0.04	0.035
Alfvén speed v_A	0.085	0.017
Alfvén Mach number M_A	1.65	2.855
Sonic Mach number M_s	3.16	1.424
Magnetosonic Mach number M_{ms}	1.463	1.272

`Loaded Simulation Box Information`

grid size		$\Delta = 0.2R_E = \Delta x = \Delta y = \Delta z$
Time Step		$\Delta t = \Delta_x/\Delta_v = 7.08$
Simulation box size		$(305 \times 225 \times 255)\Delta$
# of pair-particles		7×10^7 ion/electrons pairs
Ion to electron mass ratio		64
Particle density		$n_i = n_e = 4/\Delta^3$

Table 2. Normalized solar wind parameters at the initial state and after 3700 Δt in the solar wind for both ions and electrons for non-radial IMF.

2.2 Initial conditions

In IAPIC, the spatial and temporal scales (mass ratio and charge to mass ratio, etc ...) are chosen in order to be able to regenerate MHD large-scale classical structure of the Earth's magnetosphere (e. g., Omidi et al., 2004). For their modeling, Samsonov et al. (2017) used MHD and Community Coordinated Modeling Center (CCMC) resources, while the observational data are obtained from ACE, THEMIS and WIND spacecraft. Samsonov et al. studied the impact of non radial IMF on the magnetopause size and shape. Contextually, in the current study, we used the physical parameters they used in their MHD initial conditions and scaled them to the IAPIC initial condition values not only for non-radial IMF (where

242 B_x and B_y are dominant over B_z), but also for purely radial IMF (where B_y and B_z are
243 absent). The radial IMF is an additional case included to study differences and similarities
244 with the non radial nature of IMF on both magnetopause's shape and size and their role in
245 creating dawn-dusk asymmetries. The initial conditions of Samsonov et al. (2017) and our
246 two IMF orientations are then tabulated in Table 3.

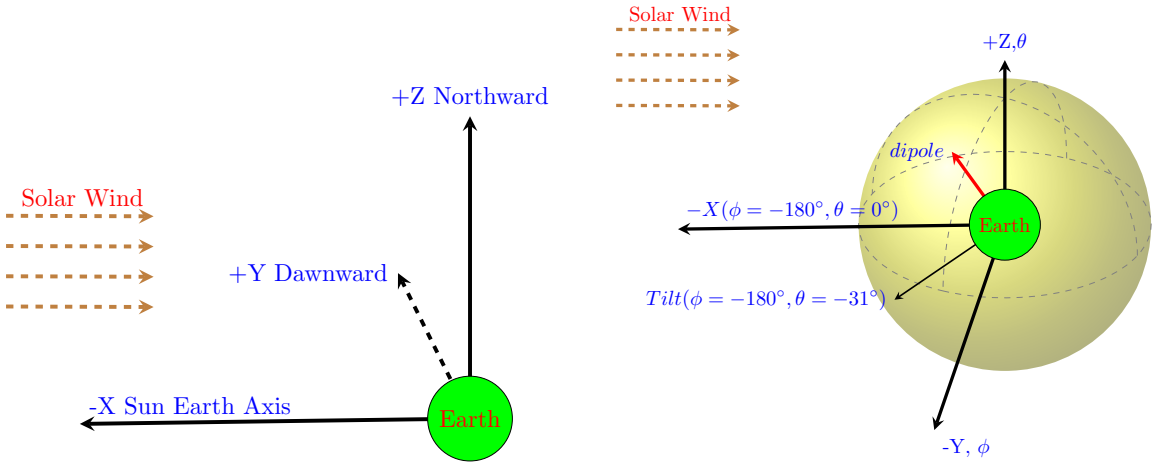

Figure 1. Code coordinates scheme (left) and spherical coordinates illustration used in MP derivation(right)

Table 3. MHD initial conditions and their corresponding IAPIC scaled values for radial and non-radial IMF orientation(Samsonov et al., 2017).

Physical Units		Normalized Units	
Parameters	MHD	$\text{IAPIC}_{\text{radial}}$	$\text{IAPIC}_{\text{non-radial}}$
$N_{SW}(n/cc)$	2.606	4.	4.
T_{sw} (Kelvin)	32263	5×10^{-4}	5×10^{-4}
V_x (km/s)	-470.69	0.1412	0.1412
V_y (km/s)	-7.80	0	0
V_z (km/s)	-5.0909	0	0
IMF_x (nT)	-2.2	0.25	0.25
IMF_y (nT)	2.99	0	-0.34
IMF_z(nT)	0.659	0	0.075
Tilt angle	31°	31°	31°
Initial Cone Angle(θ_{Bx})	54°	0°	54°
Initial Clock Angle(θ_{CA})	77.6°	45°	77.6°

3 Simulation Results

To our knowledge, a full 3D global kinetic modeling of radial IMF impacts on the dynamics of the magnetosphere has not been published, though the backstreaming of ions in the solar wind flow has been theoretically discussed (e.g., Willis, 1978, Eq. 3). The non-radial IMF event on July, 16^{th}, 2007 observed by the THEMIS probes was chosen because it has been the subject of several detailed studies (Jelínek et al., 2010; Suvorova et al., 2010; Samsonov et al., 2017). The solar wind parameters and initial conditions were scaled for IAPIC as described in section 2. For purposes of comparison, we discuss in detail the plasma properties at the time step $3700\Delta t$ of our simulation for both full and non-radial IMF. This time step corresponds to $\approx$ 24 minutes of real time, a relatively long enough period to perform kinetic simulation of the dayside magnetosphere. In the following, IAPIC simulation results are analyzed to determine the magnetopause shape, size and location for the two IMF conditions assumed, which give us a good frame to characterize any dawn-dusk asymmetry in the system.

3.1 Magnetopause response to radial and non-radial IMF

We derive the magnetopause's size to be the location of the vertical cut of the maximum density gradient steepening (using the number density derivative to get the maximum steepening). (e.g., Garcia & Hughes, 2007; J. Lu et al., 2015). We also use the pressure balance method to derive the MP location, a technique that offers an opportunity to explicitly include kinetic effects. Basically, in the pressure balance method, the dynamic and thermal pressures counter balance the dipole magnetic pressure. Because of the magnetic field axis tilt 31° at the time of observation, the system is inherently asymmetric and the Cartesian grid used in the IAPIC simulations is not adequate to accurately derive a density gradient in most planes, particularly in the tilted magnetic equatorial plane. To overcome this difficulty, we transform our Cartesian 3D simulation box quantities (density, velocity vector, …etc, at (x,y,z) positions) into a spherical 3D domain (same quantities at (r, θ, ϕ) positions), at the price of losing data from regions outside a spherical volume of radius equal to the smallest dimension of the initial Cartesian box (Dusk-Dawn and South-North in our case). Our study does not suffer of that limitation because the dayside MP, our region of interest, is located inside the selected spherical domain. After checking that both reference frames provide the same spatial distribution of all physical quantities along Sun-Earth(OX), Dusk-Dawn(OY), and South-North (OZ) axis, we focus on deriving the magnetopause size at two key planes, namely the magnetic tilt plane $\theta = -31°$ and the plane $\theta = 0°$ that contains the Sun-Earth line.

To quantify the MP expansion, we applied Shue model (Shue et al., 1997) on our physical units initial solar wind conditions, finding a MP size equal 10.3 R_E. Therefore, this size will be used as the reference MP length in the current study. Our findings are summarized and tabulated in Table 4.

In a first step, we focus on the direction defined by $\phi = -180°$ in both planes. Using the maximum density steepening technique, we derive comparable values for the magnetopause position at (~ 10.6, ~ 11.0) R_E respectively for radial and non-radial IMF along Sun-Earth

line. We also obtain the same size when the effect of backstreaming ions is removed from the bulk flow. However, along the tilted axis contained in the magnetic tilt plane, the magnetopause positions are (11.6, 12.0) R_E with bulk flow, which also remain unchanged without backstreaming ions, respectively for the two IMF conditions.

First, we note that the different magnetopause positions derived from the IAPIC simulation are all larger than the expected magnetopause position ($\sim$ 10.3 R_E) derived from Shue model (Shue et al., 1997). We remind that this reference MP size corresponds to the initial solar wind physical parameters used in our simulations. All values derived show an expansion of the magnetopause position along the two selected axes but also sunward. The magnetopause appears to be subjected to a reduced SW pressure that allows the dipole magnetic field network to expand outward. Based on the maximum density steepening technique, it is remarkable that our model predicts the magnetopause expansion self-consistently in the range (0.7-1.7) R_E along Sun-Earth axis and magnetic tilt axis for non-radial IMF.

In the following, we explore our 3D IAPIC simulation results to try uncovering potential processes that could be at the origin of the measured expansion. Since early reports, several studies pointed to the potential impact of kinetic effects, particularly with the detection of the signature of particles streaming in a direction opposite to the solar wind (Spreiter & Alksne, 1969; Willis, 1978; Sibeck et al., 2001; Samsonov et al., 2017). As IAPIC simulations offer the access to all populations of particles (macro-particles) with specific kinetic properties, we tried to extract those particles on the dayside that move sunward, against the main impinging solar flow. That statistical sub-population of particles has its own kinetic properties and most importantly counterbalances the ram pressure of the incident solar flow, as if it was originating from the magnetosphere and flowing outward. It is important to stress that this population has kinetic properties (temperature, speed, etc) much different from the planetary ionospheric population that flows from the plasmasphere or the polar wind. In Fig.2, bulk pressures (dynamic, thermal denoted P_{dyn} and P_{thm} respectively) are shown with and without backstreaming ions to highlight the difference they make in the pressure

balance. First, we remark that the thermal pressure is dominant over dynamic pressure in the magnetosheath .P_{dyn} and P_{thm} cross P_{mag} at two points, i.e. with and without backstreaming ions included. The corresponding size of the MP is $10.8R_E$ for radial IMF and $11.7R_E$ for non-radial IMF along the Sun-Earth axis. Importantly, if the backstreaming ion effect is removed, then the magnetopause size drops down to 10.5 and $11.4R_E$ for same IMF orientations respectively. The magnetopause is also measured along the tilted magnetic axis with and without backstreaming ions and found equal to 11.9, $11.5R_E$ for radial IMF and 12.0, $11.6R_E$ for non-radial IMF, respectively. To summarize, these findings are tabulated in Table 4. It is worth notice that the expansion ranges when using the pressure balance method for deriving the MP size is slightly different from that using the density steepening method. For example, The MP expansion rate is 0.5-$1.4R_E$ for radial and non-radial IMF along Sun-Earth axis, compared to 0.3-$0.7R_E$ derived by maximum density steepening method. The difference between the two measurements is 0.2-$0.7R_E$. The expansion range is 1.6-$1.7R_E$ as derived by pressure method compared to 1.3-$1.7R_E$ as measured by density steepening method respectively along tilted magnetic axis. With only a difference between the two methods of $0.3R_E$ for radial IMF and similar values for non radial IMF along the tilted magnetic axis.

In their papers (Bonifazi & Moreno, 1981b, 1981a) used ISEE2 data of 3253 ion spectra that corresponds to ≈ 90 hours, studying the density and energy of the backstreaming ions. They quantitatively characterized them into three categories. The authors used a scaling factor such that the ratio (A) of the backstreaming bulk speed to their thermal speed is ≥ 1.2 for reflected ions, and ≤ 0.8 for diffuse ions with an intermediate case $0.8 \leq A \leq 1.2$.

Here, we adopted their method to quantify the characteristics of the backstreaming ions in the dayside solar wind flow. First, a simple statistical study of the dayside populations shows that 16.5% and 20% of the solar wind bulk flow are backstreaming. For the radial IMF, we found that 72.5%of backstreaming ions are characterized by the factor $A > 1.2$, i.e. are reflected ions along the OX axis. However, only 27.5% of backstreaming ions can

Maximum Density Steepening magnetopause derivation

IMF /Axis	Sun-Earth Axis		Tilted Magnetic equator axis	
Kinetic effects	Yes	No	Yes	No
magnetopause for radial IMF	10.6 R_E	10.6 R_E	11.6R_E	11.6R_E
magnetopause for non radial	11.0R_E	11.0 R_E	12.0R_E	12.0R_E

Pressure balance magnetopause derivation

IMF/Axis	Sun-Earth Axis		Tilted Magnetic equator axis	
Kinetic effects	Yes	No	Yes	No
magnetopause for radial IMF	10.8R_E	10.5 R_E	11.9 R_E	11.5R_E
magnetopause for non radial	11.7 R_E	11.3 R_E	12. R_E	11.6 R_E

Table 4. Summary of results are tabulated as derived by density steepening method (derivative of number density) and pressure balance methods for both IMF orientations. The values are measured on both Sun-Earth Axis and magnetic tilted axis. The kinetic effect is when the bulk flow is considered, and its absence when inflow only is considered. The reference size for these values is $10.3R_E$.

be characterized as intermediate ($0.8 < A < 1.2$). see Fig. 9-(a). For the non-radial IMF case, we found a totally different characteristics for the backstreaming ions. There are only 21.6% reflected particles, and 31.4% intermediate particles and 47.0% diffuse particles along the same OX axis. To follow up the impact of the tilt axis on the particles populations, we also conducted the same statistical analysis on the magnetic equator tilt axis. We found for radial IMF that 59% reflected ions and 41% in the intermediate phase. On the other hand, the backstreaming ions are characterized as 23.5% for reflected ions, 53% for intermediate case, and finally 23.5% for diffuse ions. In Fig. 9 we found that for radial IMF, on both axis, most of the backstreaming ions are in the reflection mode, with small percentage in intermediate mode at the bow shock. On the other hand, for non-radial IMF, on both axis, backstreaming ions are in intermediate and diffuse mode in the solar wind, but the reflection mode appears to be dominant around the bow shock.

In the following, we track the magnetopause shape for both IMF orientations in two different locations. In order to handle the complex geometry of the tilted dipole, we use spherical coordinates such that ϕ=-180° at the dayside standoff distance, (θ =0) along Sun-Earth Axis and (θ=-31) along the magnetic tilt axis. In that frame, we track the shape every 20° along ϕ in two different axes (e.g., Fig.3). The MP shape for the two IMF orientations is constructed in the XY-plane and in the magnetic equator that both contain the dusk-dawn direction. In Fig.3, the MP is shown in the half-plane that contains dawn (positive Y), so that the asymmetry between dusk and dawn clearly appears using a mirror image of the MP shape in the dusk half-plane that is over-plotted on the dawn half-plane. For example, Fig.3 (a) and (b) show clear dusk-dawn asymmetry for the two selected planes (i.e. XY and magnetic equator planes). It is noticeable that the size of the MP shape strongly extends up to $\approx 15R_E$ along both dusk and dawn directions.

On the other hand, for non-radial IMF, the MP shape is shown in panels (c) and (d). The MP shape in panel (c) is squeezed earthward in dawn direction down to $7.5R_E$ with a dynamic nature structure of this portion of the MP. It is reasonable to anticipate that this reduction of the size in dusk-dawn is attributed to the strong impact of B_y. While the dusk portion of the MP shows clear asymmetry with spread out length of $\approx 12R_E$. In Fig.3 (d), we have a peculiar quasi-symmetric MP shape in the magnetic equator with a size $\approx 11R_E$ on down/dusk. We don't exactly know why this shape takes this form, but we suspect dual effects between B_y and the strong plasma current sheet that originates in the magnetotail. It seems that B_y pressuring the boundary of the MP on the flanks are encountering the pressure of the current sheet at the tilted magnetic axis.This effect is absent in the radial IMF.

In Fig.4, the linear densities for both IMF orientations are plotted in three different directions. For purely radial IMF Fig.4-a, ions and electrons are over-plotted along Sun-Earth line (OX-upper panel) from -20 to $-10R_E$ measured at Y=Z=0, Dusk-Dawn line(OY-middle panel) from -20 to -20 measured at X=$12R_E$ and Z=0, and South-North line(OZ-

lower panel) measured at X=12 R_E and Y=0. Densities in OY, and OZ panels are aimed to show the density profile just outside the MP position take at -12R_E. Vertical dashed line in the upper panel shows where the densities are plotted in the other two directions. Fig.4 shows the quasi-neutrality of the solar wind. The ions and electrons are correlated with no charge separation. Also, it is found that along OY and OZ taken just outside the MP there is apparent asymmetry at both dusk-dawn and south-north direction.

Similarly for non-radial IMF is plotted in Fig.4-b, in the OX plane, we notice a hump/heap just outside the bow shock at $\approx -16R_E$. We track plasma backstreaming at that distance and only little fraction is noticed. Its nature is reflection, in according to the characterization of backstreaming ions reported in Fig. 9. The plasma jump at -16R_E is factor 2 that is noticed when we plot the linear density along OY and OZ (not shown in the plots).

The linear density along Dusk-Dawn shows the asymmetric boundary layer structure with higher density on the dawn side than on the dusk side while in the South-North direction the linear density shows a high peak of plasma of 1.5 times higher in the south region than in the northern one.

The other major components of the solar wind dynamics is its velocity modulus that is shown in Fig.5 in the same order. The density hump in Fig. 4-b corresponds a velocity decrease in the corresponding sub-figure in Fig.5-b.

To better visualize asymmetries on large scales of the system, contour plots show a 2D cut of the plasma density distribution and magnetic field topology in 3 planes as shown in Fig.7 & 6. It is found that the planet tilt (31°) has a major impact on the global macro-structure of the magnetosphere in the simulation box of size ($\approx 60 \times 40 \times 40$ R_E). In Fig.7, panels a, b, and c are the 2D contour plot for plasma distribution along Sun-Earth axis, Dusk-Dawn axis, and South-North axis for radial IMF. Respectively panels d, e, and f are for non-radial IMF. In Fig.7-a, the planet tilt is clearly depicted. When the forefront of the

solar wind coplanar inflow approaches the magnetosheath, it hits the upper boundary of the magnetopause before the tilted magnetic axis, which makes the plasma override the boundary there before it reaches the lower boundary. This results in squeezing the magnetopause at high latitude and relaxes it in lower latitude thus making it flares out in the nightside at around $20R_E$ (see also Fig.3-a). There is around $6R_E$ vertical distance between the Sun-Earth and the tilted magnetic axes. Ionosphere is not included in the current study, while particles entry inside the magnetosphere is seen up to $5R_E$. The plasmasphere is shown up to $7R_E$. In Fig.7-d showing the plasma distribution for non-radial IMF, there is a plasma hump of $\approx 2.3R_E$ thickness between -17 and -14.5 along the Sun-Earth line and extended curve-linearly from -12 (south) to 7 (north) in a dome-like shape. It is not clear what causes this hump that is absent in the radial IMF case at the same time step. The dynamic pressure at both cusps is relatively equivalent contrary to the radial case. The relaxation of the southern part of the magnetosphere showed denser plasma population up to $30R_E$ tailward and flared in toward north at around $25R_E$. The cavity around the planet position is smaller and more confined in the non-radial IMF than the radial IMF case.

Besides that, the 2D plasma distribution in the equatorial plane for radial IMF (Fig.7-b), shows the impact of the dipole tilt on the plasma distribution in both dusk and dawn directions. It is found that the magnetosheath contracts under the pressure of large populations in the bow shock which is larger on the dusk side than on the dawn side. Furthermore, particle entry inside the magnetosphere is largely distributed around the planet making the cavity reaches $\pm 5R_E$ on South-North direction and around $3R_E$ tailward, with plasma tube along the Sun-Earth line up the planet position. While on the other hand, the effect of B_y for the non-radial IMF in Fig.7-e, shows the compressed magnetopause on both locations of dusk and dawn along OX and tilted magnetic axes. The cavity around the planet is more confined and reduced in size to $\pm 3R_E$ along south north and $\approx 1.4R_E$. The magnetospheric structure in the Dusk-Dawn plane for radial IMF (Fig.7-c) shows denser plasma in the dawn sector from 10 to 20 R_E than on the dusk side from -10 to -20 R_E, while in the northern sector of the magnetosphere there is a denser plasma that extends from around 10 to $17R_E$

but not regularly structured with same thickness in the southern sector. It appears that there is a finger like structure (particle entry) at around $5R_E$ on the dusk side that extends to around $1R_E$ in the cavity around the planet, on the other hand, for non-radial IMF the plasma distribution contour shows smaller cavity size and denser plasma on the dusk side, with a large plasma structure starting at $10 - 20R_E$ dawn and $10R_E$ north and extends to $20R_E$ downward (Fig. 7-f).

Furthermore, Fig.6 shows the corresponding magnetic field topology of Fig.7 respectively. This figure sheds light on the differences and similarities between two IMF orientations along three different planes. In Fig.6-a the radial IMF field lines along OX are horizontal at $-20R_E$ and $\pm 3R_E$ along South-North direction and seen curled at $\pm 10R_E$. At the magnetopause position, the field lines divert at f(x,z)=$(-10, -8)R_E$. At dayside magnetosphere, there are two potential magnetic reconnection sites(MR) sites approximately located at f(x,z)=$(0.5, -12)\&(-7.6, 11.9)R_E$. The magnetic field line topology shown in Fig.6-d is horizontal in the undisturbed SW, this was not the case in Fig.6-a. This difference is attributed to the impact of B_y. Potential MR sites are seen also at f(x,z)=$(-10.6, 9.1)\&(0.5, 10.1)R_E$. Constant attention should be made when looking at Fig.6-b, taken in the equatorial plane, because of the dipole tilt, what is shown here for radial IMF is the high latitude magnetopause along OX in Dusk-Dawn direction. It is found that field lines from IMF connect to dipole field and permit particle entries at that latitudes. The wavy structure in the nightside (not the focus of the current study) indicates a complex current system induced at that distance. A potential MR site is shown at f(x,y)=$(-7.6, 9.9)R_E$. The curling of magnetic field lines at f(x,y)=(5,-15), (-15,-7)R_E corresponds to the plasma dynamics shown in Fig.7-d. Same in Fig.7-e for non-radial IMF, the curled magnetic field lines at a latitude corresponding to $\approx 6R_E$(north) are directed toward dusk-midnight direction. Potential MR sites are at f(x,y)=(4.4,5.9), (-8.6,0.1), (3.5,-7.9)R_E. In Fig.6-c, the dawn side magnetic field topology shows more extended structure of closed magnetic field lines until $\approx 14R_E$ toward dawn and reach up to $12R_E$ northward. In contrary, the non-radial IMF case in Dusk-Dawn plane (Fig.6-f) shows different structure,

where the extension of field lines is more important on the dusk side, but there are large scale connections of planetary and interplanetary magnetic field lines and clear MR position at f(y,z)=(-9.6,9),(3.4,-11.4)R_E.

The solar wind species temperature is important to track the particles entry from the cold component, the solar wind origin, to hot component of the magnetosheath plasma. The T_i/T_e is approximately conserved at the MP boundary. (Wing et al., 2014). Moreover, the T_i/T_ei ratio is thoroughly investigated by (Lavraud et al., 2009) . In the current paper, the ion-to- electron temperature ratio (T_i/T_e) of the impinging solar wind is depicted in Fig.8. For radial IMF Fig.8-a, the ion temperature T_i slightly fluctuating in the solar wind until it increases by a factor 2 between -15 to-12 R_E then decreased downstream before it increased again in the magnetosheath until it reached the MP position before abruptly jumped inside the magnetosphere. While on the other hand the electron temperature T_e in the magnetosheath maintains constant value, with factor 1.2 than electron temperature in the solar wind. The average (T_i/T_e) ratio in the magnetosheath is $\approx$= 1.1. Moreover the temperature profile in the non-radial IMF Fig.8-b. is different from that purely radial IMF. The T_i start constantly increasing at $-15R_e$ including the bow shock and the magnetosheath. The T_i ratio in the sheath to the solar wind is a factor 4. The T_e on the other hand, start increasing at -16R_E up to downstream and continued inside the magnetosheath. The average (T_i/T_e) ratio in the magnetosheath is $\approx$ 2. more discussion about temperature ion-to-electron ratio and temperature anisotropy is in section-(4)

The temperature anisotropy was studied extensively in the past(Gingell et al., 2015; Karimabadi et al., 2014; Treumann & Baumjohann, 2013). In the current paper, we were able to derive the solar wind species temperature anisotropy. In Fig.8-c for radial IMF, the average ion temperature anisotropy $T_{\perp i}/T_{\parallel i}$ in the dayside magnetosphere is $\approx$ 1.7, and inside the magnetosheath this ratio reaches $\approx$ 2.7, the maximum ratio is found at the bow shock with a factor of 3.3. It is found that the temperature anisotropy where the solar wind plasma departs their thermal equilibrium in the solar wind is almost isotropic. As per the

491 average electron temperature anisotropy $T_{\perp e}/T_{\|e}$, it is found in the dayside magnetosphere
492 equal ≈ 2.2 which is almost the same inside the magnetosheath. In Fig. 8-d, for non-radial
493 IMF orientation, the anisotropy average for ions in the dayside magnetosphere is $T_{\perp i}/T_{\|i}$
494 ≈ 6 for ions and ≈ 1.6 for electrons. In the magnetosheath the $T_{\perp i,e}/T_{\|i,e}$ for ions and
495 electrons is 3.2 and 3.4, respectively. These results will be discussed in section 4.

496 3.2 Dawn-Dusk asymmetry in the dayside magnetosphere under the influ-
497 ence of radial and non-radial IMF

498 . The large scales results reported above all indicate systematic asymmetries in Dusk-
499 Dawn and South-North directions for the two IMF orientations. In the following, we try
500 to quantify those asymmetries, particularly in the Dusk-Dawn direction for the radial and
501 non-radial IMF cases we have simulated. Figures, 3, 4, 7-(panels, b, e, c, and f), and 11
502 clearly show asymmetry in the Dusk-Dawn direction.

503 Fig.7-b,e show the Dusk-Dawn asymmetry along the Sun-Earth direction (OX) and
504 Fig.7-c,f show the asymmetry along the Dusk-Dawn (OY) and South-North(OZ) directions.
505 Linear density plots are shown in Fig.4, middle panel, and plasma boundary layers in the
506 equatorial. The asymmetry in the South-North planes can be seen in Fig.4 lower panel. In
507 Fig.11, some solar wind parameters i.e. N_i, T_i, T_e, V_i, B_x,B_y and B_z are plotted at three
508 different locations for each IMF orientation. Two of which are at $\pm 6 R_E$ on both sides of OX
509 axis, and the third along the Sun-Earth line from -18 to 10.8 and 11.7 R_E for radial and
510 non-radial IMF. More details are given in the next section 4. In Table 5 measured values of
511 the solar wind parameters are tabulated.

512 In Fig.11, left panel shows the radial IMF parameters. Ion plasma is denser along OX
513 in the dusk side than on the dawn side in the solar wind up to the magnetosheath. For
514 non-radial IMF, right panel, density in the dusk side got a factor 2 jump in the bow shock
515 region for the density in both dawn and along OX axis. For ion temperature T_i, we noticed
516 that it is hotter in the dawn side only in the solar wind before the foreshock region, then it

cools down and the dusk temperature increases. The up and downstream ion temperature long OX is close to that along dusk for radial IMF. For non radial IMF, we noticed that there is hotter plasma in the solar wind along dusk direction. Then, T_i is correlated with the other directions, but still show asymmetry. On the other hand, T_e is hotter in the solar wind along dusk direction, and then cooles down in the downstream compared to that in the dawn and OX direction. Ion velocity (V_i), decelerates at both dusk and dawn directions though it is faster than V_i on OX direction for radial IMF. For non-radial IMF, the deceleration of solar wind in the downstream is correlated along OX and dusk direction but it s steady along dawn. For all parameters considered, there is an apparent dawn-dusk asymmetry.

Solar wind parameters for radial IMF

Parameter	Dawn ($Y = +6R_E$)	Dusk ($Y = -6R_E$)	OX (Y=0)	Dawn/dusk
N_i	8.148	8.076	7.978	0.988
T_i	0.003	0.004	0.007	1.704
T_e	0.156	0.192	0.218	1.132
V_i	0.054	0.043	0.038	0.878
B_x	0.226	0.105	-0.023	0.218
B_y	0.193	0.141	-0.216	1.532
B_z	-0.033	-0.067	-0.053	0.790
Solar wind parameters for non radial IMF				
N_i	8.308	4.176	3.206	0.768
T_i	0.002	0.002	0.004	1.946
T_e	0.153	0.144	0.161	1.118
V_i	0.052	0.045	0.021	0.456
B_x	0.130	0.248	0.156	0.631
B_y	-0.442	-0.384	-0.462	1.202
B_z	0.003	0.152	-0.008	0.054

Table 5. To monitor the Dusk-Dawn asymmetry, plasma parameters are calculated and averaged at the derived position of the magnetopause at $10.8R_E$ at subsolar point, $8.5R_E$ at dusk flank, and $6R_E$ at dawn flank for radial measured at $\pm 6R_E$. While data is derived for non radial IMF as$11.7R_E$ at the subsolar MP, $8.6R_E$ at the dusk flank, and $6.9R_E$ at the dawn flank respectively.

4 Discussion and Analysis

As described in section 3.1, we derived the MP position (10.6,11.0) R_E along the Sun-Earth line for purely and non-radial IMF, respectively (using the location of the maximum number density gradient). In addition, we have shown that PIC simulations offer the possibility to isolate backstreaming ions from the pool of particles in the box simulation. This process allows us to derive their contribution to the dynamic and thermal pressures in the

dayside magnetosphere. It is important to stress that other complex effects could be induced by the presence of those backstreaming particles, like induced currents and fields, that will be considered in a future study. Elimination of the contribution of backstreaming ions in the ensemble average of the plasma properties increases the resulting system pressure and consequently moves the magnetopause location toward Earth.

Using the balance between ram pressure and magnetic pressure, (e.g., Willis, 1978, Eq. 3) we were able to derive the MP size in different planes with and without backstreaming ions (Table 4). These calculations reveal the impact of backstreaming ions in reducing the solar wind dynamic pressure allowing for MP expansion by 0.3-0.4R_E. All our findings above also suggests the important results that by neglecting ions kinetic effects, MHD simulations implicitly overestimate SW pressure in the foreshock and underestimate the MP size.

For instance, the MP expansion range derived here is consistent with the expansion observed by THEMIS spacecraft for the event of July,16^{th}, 2007. To match the observed expansion, Samsonov et al. (2017) were forced to modify the solar wind properties, propagated from WIND and ACE *in situ* measurements, of their boundary conditions in order for their MHD model. This means that a non negligible fraction (up to 40%) of the observed expansion that is due to backstreaming particles was inadvertently attributed in their study to a change in the SW upstream properties.

We conclude that the dynamic pressure of backstreaming ions contributes significantly to the expansion/compression of the magnetopause. Note that when the magnetopause is derived from the density maximum steepening, the effect of the backstreaming ions was absent. This indicates that the main driver of the expansion of the magnetopause is the upstream reduction of the solar wind dynamic pressure in the foreshock. More generally, the insensitivity of the MP size to the density of backstreaming ions confirms the conclusions reported in (Samsonov et al., 2020, Eq. 2), that density and velocity (dynamic pressure) might have different contributions to the effective values of the dynamic pressure component in the pressure system balance used in driving the magnetopause position. This appears

clearly in our results in Table 4.

The presence of backstreaming particles should also affect the temperature anisotropy in the dayside magnetosphere. Using THEMIS measurements, (Wang et al., 2012) showed how the T_I/T_e ratio changes in the magnetosheath and the plasma sheet. They showed that $T_I/T_e \approx 4-12$ in the magnetosheath. Other studies statistically examined the T_i/T_e in different regions in the magnetosphere to find a ratio $\approx$ 6-12 (Phan et al., 1994; Paschmann et al., 1993). On the other hand the T_I/T_e ratio was as low as ≈ 3 as reported in (Lavraud et al., 2009) when the authors studied this ratio at the flank magnetosheath. In the current paper, we show in Fig.8-a and (b), the ion and electron temperature ratio in the dayside magnetosphere. The average T_i/T_e ratio in the magnetosheath is found 1.7 and 1 for radial and non-radial IMF (Dimmock et al., 2014, 2015). The T_i/T_e ratio for non-radial IMF is ≈ 1 but it reached an average of 5 if taken from -18 to -10 R_E. On the other hand, (Grygorov et al., 2017; Samsonov et al., 2012) showed that the temperature anisotropy in the magnetosheath controls the pressure distribution near the magnetopause. Here we found that the ion temperature anisotropy ratio is about 2 in the magnetosheath for radial IMF, and about 6 for non radial IMF (Fig.8-c,d), consistent with (Wang et al., 2012). Analysis of the temperature distributions will be used in future work to study microinstabilities and reconnection.

To characterize the kinetic properties of the backstreaming particles, we first use the nomenclature of (Bonifazi & Moreno, 1981b). We found that for the radial IMF, the percentage of reflected ions ($A > 1.2$) in the backstreaming population is 72.54%, while intermediate reflected ($0.8 < A < 1.2$) ions represents 27.45% (see Fig. 9-(a)). For the non-radial IMF case, we found that backstreaming ions have totally different characteristics as only 21.56% of them are reflected particles, 31.37% are intermediate particles, and 47.05% diffuse particles. In Table 6 we show the speed of backstreaming bulk velocity in real physical units in accordance with the characterization factor reported in (Bonifazi & Moreno, 1981b). It is

found that the backstreaming ions are faster along the tilted magnetic axis than the sun-earth axis for both IMF orientations. It is the same case for the thermal speed of those ions. While the bulk flow speed is faster for radial IMF along the sun- earth line than the tilted magnetic axis, on contrary, the bulk flow speed is faster along tilted magnetic axis than the sun-earth axis for non-radial IMF. Note that 16.5% and 20% of the bulk flow are backstreaming ions for radial and non-radial IMF respectively.

To better understand the kinetics of the distribution of the backstreaming ions, we show the velocity distribution function (VDF) of solar wind ions along the Sun-Earth line as far as $-20R_E$ (Fig.10). For the purely radial IMF case, a substantial fraction of VDF spatial distribution of backstreaming ions is found in the three planes (XZ, XY and YZ) whereas only a small fraction is obtained for non-radial IMF especially in the YZ plane. The VDF in Fig.10-a shows reflection of the plasma sunward and southward for radial IMF, with minor reflection for non radial IMF with a lot of diffuse northward and earthward direction as confirmed by Fig. 9. It is also found that in the equatorial plane for both IMF orientations, that the reflection of backstreaming ions are dominant over their diffuse and intermediate for radial than non radial IMF. While on the other hand in Fig.10-c and f, the spatial distribution of ions are reflected mostly toward south and sunward for radial and mostly toward north for non radial IMF.

The second major finding of this study is the Dawn-Dusk asymmetry. Uncovering its origin is important for better understanding, modeling and prediction of space weather phenomena (e. g., S. Lu et al., 2016). Asymmetry is observed by Cluster spacecraft in north-south magnetotail planes (Haaland et al., 2017; Samsonov, 2006) and in dawn-dusk planes (A. P. Walsh et al., 2014; Samsonov, 2011; Dimmock et al., 2017; Turc et al., 2020). Both observations and numerical simulations have revealed that the magnetopause size is a function of IMF strength and orientation, and solar wind dynamic pressure, which by turn modify the magnetopause shape and generate dawn-dusk asymmetries (Liu et al., 2019). Using data from IMP 8 and ISEE,1, ISEE, 3 and WIND, Paularena et al. (2001); Dimmock

Number density data

	Radial	Non radial
# inflow ions	5.38958×10^7	5.21372×10^7
# backstreaming ions	8.87744×10^6	1.07256×10^7
percentage	16.5%	20%

Backstreaming Ions Characteristics

	Radial		Non radial	
	OX	Tilt	OX	Tilt
reflected ions	72. %	58.%	22.%	24.%
intermediate ions	27. %	41. %	31.%	53.%
diffuse ions	1.%	1. %	47.%	23.%
$V_{bp}(km.s^{-1})$	373	392	294	346
$V_{thm}(km.s^{-1})$	254	255	321	332
$V_{sw}(km.s^{-1})$	287	254	233	248

Table 6. The ratio of backstreaming ions to bulk flow of the number density for both IMF orientations is shown in the upper panel. The backstreaming ions are characterized with three categories (see Fig. 9). Based on scaling factor ((Bonifazi et al., 1980)) the backstreaming ions are reflected, intermediate or diffuse. V_{bp} bulk flow of the backstreaming ions, V_{thm}, their thermal speed and the solar wind velocity V_{sw} are shown in the lower panel for both IMF orientations along OX and Tilt axis.

et al. (2014) showed a significant dawn-dusk asymmetry in the Earth's magnetosheath which is larger on the dawn side than on the dusk side. They also showed that the IMF orientation impacts density asymmetry in dawn-dusk direction. Paularena et al. (2001) reported same kind of asymmetry in different regions in the dayside magnetosphere in Sun-Earth and Dusk-Dawn planes. In their recent study, Turc et al. (2020) discussed the magnetosheath asymmetry in terms of IMF, solar wind density, velocity by using Vlasiator hybrid code (Palmroth et al., 2018). They found that magnetic field asymmetry and density variability in the magnetosheath are stronger when IMF tends toward a radial direction. Similarly, using IAPIC, the dawn-dusk asymmetry in the magnetosheath and in the solar wind is investigated. In our work, the MP shape in Fig. 3, shows how asymmetric the dawn-dusk are. A result that is confirmed in Fig. 11, IMF, density, temperature and ion velocity are tested at the dusk-dawn flanks asymmetry in the magnetosheath. The magnetosheath, left to the vertical blue dashed line, all the parameters are asymmetric. This is consistent with (Turc et al., 2020). The vertical red dashed line shows the MP position at $-6R_E$ at the dusk flank at distance 8.5,8.6 for radial and non-radial IMF. Whilst the vertical green dashed line shows the position at $+6R_E$ at the dawn flank. The solar wind parameters at the MP at subsolar point, dusk and dawn flanks are then quantified and tabulated in Table 5.

Finally, our analysis of the location, shape and size of the MP with the techniques developed for that purpose, in addition to the ability to quantify plasma parameters in 3D to track asymmetries in the dusk-dawn and south-north direction our code is applicable to planetary and exoplanetary magnetospheres. Furthermore, our findings can also contribute to alternative methods for a better analysis of soft x-ray imaging of the magnetosphere (Sibeck et al., 2018) in a complementary manner. This includes the MP, the cusp dynamics, the magnetosheath that is related to density structure which can be deduced from soft x-ray observation.

Most current support to the SMILE mission is based on MHD modeling (SMILE working group). In light of the results obtained so far (see Figs. 2 and 3 , and Tables 4), our

global 3D electromagnetic kinetic code is providing another point of view on the range of expected boundary locations under various solar wind flux. An accurate estimation of those boundary locations are key to interpret X-ray signal that will be detected by SXI, the SMILE X-ray detector. In addition, our simulations provide details about ions kinetic properties locally and on global scales (eg. Fig. 4), an additional tool for coupling plasma properties that will be detected by the light Ion Analyser (LIA) and large scale structure that will imaged by SXI. In light of the results obtained so far, we propose IAPIC, as a global 3D electromagnetic kinetic code to simulate the MP, the cusps, and the magnetosheath, which should enhance the science return of space missions like the CSA − ESA SMILE mission.

5 Summary and Conclusion

We have utilized a three-dimensional kinetic particle-in-cell code (IAPIC) to determine the size, shape and location of the Earth's magnetopause with a dipole tilt of 31° in response to solar wind conditions of radial (B=Bx) and non-radial (Bz < Bx, By) IMF, covering the range of quasi-radial IMF that takes a cone angle between 0 and 50°. The simulations show the MP expanding anti-sunward and predict asymmetric magnetosphere in both IMF orientations.

Using a reference MP size (10.3 R_E) independently derived from (Shue et al., 1997), the findings of this study are summarized as follows:

1. The MP expands from 10.3 to 10.8R_E for the bulk flow and to 10.5R_E when effect of the backstreaming ions are dropped from calculations along OX axis for radial IMF. In other words, 40% of the observed expansion is due to backstreaming solar wind particles. Moreover, along tilted magnetic axis, the MP expansion is 10.3 to 11.9 and 11.5 respectively.
2. For non radial IMF, the expansion is from 10.3 to 11.7 and to 11.3R_E for bulk flow and 10.3 to 12.0 and 11.6R_E when backstreaming ions are not accounted for in the flow.

3. The expansion rate for non radial IMF is 1.4 and $1.7R_E$ along OX and tilt axis for bulk flow is comparable with the average expansion of 1.3-1.5R_E reported from Themis observations (Jelínek et al., 2010; Suvorova et al., 2010), without being forced to modify the input solar wind parameters as done by MHD model (Samsonov et al., 2017).
4. The expansion rate along tilted magnetic axes is larger for both IMF orientation than OX plane. This result is explained by the presence of the current sheet that is naturally predicted by our kinetic simulation in the magnetic equator. For reference, the presence of the current sheet indicates that an additional plasma, entering from the tail, will provide an additional pressure from inside (opposite to SW pressure) that explains why our MP position is always larger along the tilt than the OX axis in the XY plane.
5. The backstreaming ions contribution to the bulk flow is 16.5%, and 20% for radial and non-radial IMF respectively along the OX axis in the dayside magnetosphere.
6. When deriving the MP position using the maximum density steepening method, the backstreaming ions(characterized and quantified in this study) do not impact the measured size of the MP for both IMF orientations along both OX and tilted axis.
7. In contrast, when the magnetopause is derived using pressure system balance, backstreaming ions expand the magnetopause by $0.3 - 0.4\ R_E$ (Table 4).
8. The difference between magnetopause derivation using maximum density steepening (Garcia & Hughes, 2007; J. Lu et al., 2015) and the pressure systems balance using definition of dynamic pressure as in (e.g., Willis, 1978, Eq. 3) is consistent with the conclusion drawn by (Samsonov et al., 2020) that density and velocity act differently as a component of dynamic pressure in the pressure system balance. In our study, we also considered the effect of thermal pressure in the magnetosheath in the pressure balance.
9. We present new results showing the magnetopause shape in spherical polar coordinates for the two IMF directions. This new technique along with the magnetopause

derivations in Table 4 and Fig. 2 enables us to anticipate the sizes, shapes and locations of magnetopause for all magnetized planets, including magnetized exoplanets. Additionally, this technique accounts for the backstreaming ion contribution to the data used to derive the magnetopause shape, a key information that is not available with other types of simulations.

10. The current study enabled us to derive the solar wind temperature anisotropy, thus paving a research road to study kinetic microinstabilities in the solar wind-magnetosphere coupling (see Figs. 8). For non-radial IMF, $T_\perp/T_\parallel$ is large and equal ≈ 6 for ions and ≈ 1.6 for electrons. On the other hand, the $T_\perp/T_\parallel$ for radial IMF equal to 1.8 and 2.2 for ions and electrons respectively. The $T_{\perp e}/T_{\parallel e}$ ratio can be employed to predicts whistler waves like those observed by MMS((Le Contel et al., 2016)). Temperature anisotropy linked to magnetic reconcention is widely discussed i.e. (Gingell et al., 2015),
11. The 3D velocity distribution function (Fig. 10) shows that backstreaming ions appear upstream to distances of about $-20R_E$. Draping of the IMF, and temperature anisotropy in the magnetosheath, give rise to a complex structure that results in the asymmetry observed in the dawn-dusk and north-south directions. The dawn-dusk asymmetry is quantified in the current paper by tracking solar wind parameters at $\pm 6R_E$ cut parallel to OX plane. In Table 5, the solar wind parameters are measured at 10.8 and $11.7R_E$ along the three parallel planes. Derived numbers at the MP position show the asymmetry numerically. In Fig. 11, the asymmetry is depicted for both IMF orientations as seen by the different color lines in each sub-figure.
12. In light of the results so far obtained, our findings are considered an additional and key modeling supports to future near-Earth exploration projects, in additions to outer planets moons and magnetospheres. For example, the newly developed technique to map the MP shape and position, or the ability to track backstreaming ions and their characterizations and their kinetic impact on the plasma flow will contribute

721 to deepen our understanding about the kinetic behavior of plasma in the solar wind
722 magnetosphere coupling and the study of exoplanets magnetospheres.

723 **Future Directions**

724 Radial and non-radial conditions are relatively infrequent configurations of the IMF at Earth,
725 but closer to the Sun, the Parker spiral becomes more and more radial. This suggests that
726 radial IMF conditions are more common at Mercury, which has recently been investigated
727 by MESSENGER and will soon be visited by the BepiColombo spacecraft. Furthermore,
728 Mercury's magnetosphere is much smaller as the magnetopause standoff position is only at
729 about $2R_M$ (R_M being the Mercury radius) and the ion gyroradius is about the size of the
730 planet. Finite Larmor radius effects are expected to play an ever more important role than
731 in the Earth's case (e.g., Johnson et al., 2014; Paral & Rankin, 2013). Mercury is therefore
732 a natural laboratory for investigating radial IMF and related kinetic effects and we will
733 prepare simulations in advance of BepiColombo's arrival at Mercury. Planets even closer to
734 their stars are common in the galaxy (NASA Exoplanets Archive $doi = 10.26133/NEA2$),
735 suggesting that, particularly around cooler M- and K-type stars, radial IMF may be a
736 common condition. This impacts the structure of their magnetospheres and may influence
737 the escape of planetary atmospheric and ionospheric constituents over time. The kinetic
738 aspect of our approach is particularly sensitive to the dynamics of the bow shock, which
739 may be highly variable in the neighborhood of a small star (Cohen et al., 2015), potentially
740 producing accelerated particles and observable radio emissions (Cohen et al., 2018). One
741 more issue that will be considered for near future work is the impact of the magnetosphere-
742 ionosphere-magnetosheath coupling on magnetopause location. We have tracked in the
743 past $H^+$and O^+ ions outflow from the ionospheric origin in the dayside magnetosphere
744 (S. M. Baraka & Ben-Jaffel, 2015). IAPIC can also be used to study outflow of plasmasphere
745 low energy ions.

746 **Acknowledgments**

747 This work is carried out using binary data generated by IAPIC, a pic code that is a mod-
748 ified version of the Tristan code that is available to the public through GitHub: `https://`
749 `github.com/ntoles/tristan-mp-pitp`. THEMIS, ACE, and, Wind data are available at

http://amda.cdpp.eu/. The used data for generating results is available at ((https://doi.org/10.48392/bar-001). S Baraka acknowledges the NIA NASA grant # NNX15AE05G for supporting this research via the Living and Breathing Planet project. L. Ben-Jaffel acknowledges support from CNES under project PACES. S. Baraka thanks IAP-CNRS for using their computing resources facilities and generating the simulation data. Also S Baraka thanks Daniel Pomarede from Atomic Energy Commission, CNRS, France for providing SD-vision software .

References

Akasofu, S.-I. (1991). Development of magnetospheric physics. *Magnetospheric Substorms*, *64*, 3–9.

Akasofu, S.-I., Roederer, M., & Krimigis, S. (1982). Dawn-dusk asymmetry of the tail region of the magnetosphere of saturn and the interplanetary magnetic field. *Planetary and Space Science*, *30*(10), 1061–1063.

Artemyev, A., & Zelenyi, L. (2012, December). Kinetic Structure of Current Sheets in the Earth Magnetotail. *Space Science Reviews*, *178*(2-4), 419–440. doi: 10.1007/s11214-012-9954-5

Asbridge, J., Bame, S., & Strong, I. (1968). Outward flow of protons from the earth's bow shock. *Journal of Geophysical Research*, *73*(17), 5777–5782.

Baraka, S. (2016, April). Large Scale Earth's Bow Shock with Northern IMF as Simulated by PIC Code in Parallel with MHD Model. *Journal of Astrophysics and Astronomy*, *37*(2), 1–16. doi: 10.1007/s12036-016-9389-6

Baraka, S., & Ben-Jaffel, L. (2007, June). Sensitivity of the Earth's magnetosphere to solar wind activity: Three-dimensional macroparticle model. *Journal of Geophysical Research (Space Physics)*, *112*, 6212. doi: 10.1029/2006JA011946

Baraka, S., & Ben-Jaffel, L. (2011). Impact of solar wind depression on the dayside magnetosphere under northward interplanetary magnetic field. *Annales Geophysicae*, *29*(1), 31–46. Retrieved from https://www.ann-geophys.net/29/31/2011/ doi: 10.5194/angeo-29-31-2011

Baraka, S. M., & Ben-Jaffel, L. (2015). Magnetospheric dynamical and morphological response to multi-species plasma supply from the ionosphere: New comprehensive 3d pic simulation. *AGUFM*, *2015*, SM23B–2552.

Ben-Jaffel, L., & Ballester, G. (2013, May). Hubble Space Telescope detection of oxygen in the atmosphere of exoplanet HD 189733b. *Astronomy & Astrophysics*, *553*, A52. doi: 10.1051/0004-6361/201221014

Ben-Jaffel, L., & Ballester, G. E. (2014, April). Transit of Exomoon Plasma Tori: New Diagnosis. *apjl*, *785*, L30. doi: 10.1088/2041-8205/785/2/L30

Berchem, J., Richard, R. L., Escoubet, C. P., Wing, S., & Pitout, F. (2016, January). Asymmetrical response of dayside ion precipitation to a large rotation of the imf. *Journal of Geophysical Research (Space Physics)*, *121*, 263–273. Retrieved from https://ui.adsabs.harvard.edu/abs/2016JGRA..121..263B doi: 10.1002/2015JA021969

Blanco-Cano, X., Omidi, N., & Russell, C. (2006). Macrostructure of collisionless bow shocks: 2. ULF waves in the foreshock and magnetosheath. *Journal of Geophysical Research: Space Physics (1978–2012)*, *111*(A10).

Blanco-Cano, X., Omidi, N., & Russell, C. (2009). Global hybrid simulations: Foreshock waves and cavitons under radial interplanetary magnetic field geometry. *Journal of Geophysical Research: Space Physics*, *114*(A1).

Bobra, M., Petrinec, S., Fuselier, S., Claflin, E., & Spence, H. E. (2004). On the solar wind control of cusp aurora during northward imf. *Geophysical research letters*, *31*(4).

Bonifazi, C., & Moreno, G. (1981a). Reflected and diffuse ions backstreaming from the earth's bow shock 1. basic properties. *Journal of Geophysical Research: Space Physics*, *86*, 4397-4404. doi: 10.1029/ja086ia06p04397

Bonifazi, C., & Moreno, G. (1981b). Reflected and diffuse ions backstreaming from the Earth's bow shock 2. Origin. *Journal of Geophysical Research: Space Physics (1978–*

2012), *86*(A6), 4405–4413.

Bonifazi, C., Moreno, G., Lazarus, A. J., & Sullivan, J. D. (1980, November). Deceleration of the solar wind in the earth's foreshock region - ISEE 2 and IMP 8 observations. *\textbackslashjgr*, *85*, 6031–6038. doi: 10.1029/JA085iA11p06031

Brackbill, J. U. (2011). A comparison of fluid and kinetic models of steady magnetic reconnection. *Physics of Plasmas (1994-present)*, *18*(3), 032309. doi: 10.1063/1.3568828

Buneman, O., Neubert, T., & Nishikawa, K.-I. (1992). Solar wind-magnetosphere interaction as simulated by a 3-d em particle code. *IEEE transactions on plasma science*, *20*(6), 810–816.

Cai, D., Esmaeili, A., Lembège, B., & Nishikawa, K.-I. (2015). Cusp dynamics under northward imf using three-dimensional global particle-in-cell simulations. *Journal of Geophysical Research: Space Physics*, *120*(10), 8368–8386.

Cai, D., Li, Y., Nishikawa, K.-I., Xiao, C., Yan, X., & Pu, Z. (2003). Parallel 3-D Electromagnetic Particle Code Using High Performance FORTRAN: Parallel TRISTAN. In *Space Plasma Simulation* (Vol. 615, pp. 25–53). Springer Berlin Heidelberg. doi: 10.1007/3-540-36530-3_2

Cohen, O., Ma, Y., Drake, J. J., Glocer, A., Garraffo, C., Bell, J. M., & Gombosi, T. I. (2015, jun). THE INTERACTION OF VENUS-LIKE, m-DWARF PLANETS WITH THE STELLAR WIND OF THEIR HOST STAR. *The Astrophysical Journal*, *806*(1), 41. Retrieved from `https://doi.org/10.1088/0004-637x/806/1/41` doi: 10.1088/0004-637x/806/1/41

Cohen, O., Moschou, S.-P., Glocer, A., Sokolov, I. V., Mazeh, T., Drake, J. J., … Alvarado-Gómez, J. D. (2018, oct). Exoplanet modulation of stellar coronal radio emission. *The Astronomical Journal*, *156*(5), 202. Retrieved from `https://doi.org/10.3847/1538-3881/aae1f2` doi: 10.3847/1538-3881/aae1f2

Dimmock, A., Nykyri, K., Osmane, A., Karimabadi, H., & Pulkkinen, T. (2017). Dawn-dusk asymmetries of the earth's dayside magnetosheath in the magnetosheath interplanetary medium reference frame. *Dawn-Dusk Asymmetries in Planetary Plasma Environments*, 49–72.

Dimmock, A. P., Nykyri, K., Karimabadi, H., Osmane, A., & Pulkkinen, T. I. (2015, April). A statistical study into the spatial distribution and dawn-dusk asymmetry of dayside magnetosheath ion temperatures as a function of upstream solar wind conditions. *Journal of Geophysical Research (Space Physics)*, *120*(4), 2767-2782. doi: 10.1002/2014JA020734

Dimmock, A. P., Nykyri, K., & Pulkkinen, T. I. (2014, August). A statistical study of magnetic field fluctuations in the dayside magnetosheath and their dependence on upstream solar wind conditions. *Journal of Geophysical Research (Space Physics)*, *119*(8), 6231-6248. doi: 10.1002/2014JA020009

Dušík, Š., Granko, G., Šafránková, J., Němeček, Z., & Jelínek, K. (2010). Imf cone angle control of the magnetopause location: Statistical study. *Geophysical Research Letters*, *37*(19).

Eastwood, J. P. (2008). The science of space weather. *Philosophical Transactions of the Royal Society A: Mathematical, Physical and Engineering Sciences*, *366*(1884), 4489–4500.

Fairfield, D., Baumjohann, W., Paschmann, G., Lühr, H., & Sibeck, D. (1990). Upstream pressure variations associated with the bow shock and their effects on the magnetosphere. *Journal of Geophysical Research: Space Physics*, *95*(A4), 3773–3786.

Garcia, K., & Hughes, W. (2007). Finding the lyon-fedder-mobarry magnetopause: A statistical perspective. *Journal of Geophysical Research: Space Physics*, *112*(A6).

Gingell, P. W., Burgess, D., & Matteini, L. (2015, March). The Three-dimensional Evolution of Ion-scale Current Sheets: Tearing and Drift-kink Instabilities in the Presence of Proton Temperature Anisotropy. *The Astrophysical Journal*, *802*(1), 4. doi: 10.1088/0004-637X/802/1/4

Greenstadt, E. W., Green, I. M., Inouye, G. T., Hundhausen, A. J., Bame, S. J., & Strong, I. B. (1968, January). Correlated magnetic field and plasma observations of the Earth's

bow shock. *textbackslashjgr*, *73*, 51. doi: 10.1029/JA073i001p00051

Grygorov, K., Šafránková, J., Němeček, Z., Pi, G., Přech, L., & Urbář, J. (2017). Shape of the equatorial magnetopause affected by the radial interplanetary magnetic field. *Planetary and Space Science*, *148*, 28–34.

Haaland, S., Lybekk, B., Maes, L., Laundal, K., Pedersen, A., Tenfjord, P., … Snekvik, K. (2017). North-south asymmetries in cold plasma density in the magnetotail lobes: Cluster observations. *Journal of Geophysical Research: Space Physics*, *122*(1), 136–149.

Haaland, S., Reistad, J., Tenfjord, P., Gjerloev, J., Maes, L., DeKeyser, J., … Dorville, N. (2014). Characteristics of the flank magnetopause: Cluster observations. *Journal of Geophysical Research: Space Physics*, *119*(11), 9019–9037.

Haaland, S., Runov, A., Artemyev, A., & Angelopoulos, V. (2019). Characteristics of the flank magnetopause: Themis observations. *Journal of Geophysical Research: Space Physics*, *124*(5), 3421–3435.

Heikkila, W. J. (2011). *Earth's Magnetosphere: Formed by the Low-latitude Boundary Layer*. Elsevier.

Jacobsen, K. S., Phan, T. D., Eastwood, J. P., Sibeck, D. G., Moen, J. I., Angelopoulos, V., … Fornaçon, K.-H. (2009). THEMIS observations of extreme magnetopause motion caused by a hot flow anomaly. *Journal of Geophysical Research (Space Physics)*, *114*, 8210. Retrieved from `http://adsabs.harvard.edu/abs/2009JGRA..114.8210J`

Jelínek, K., Němeček, Z., Šafránková, J., Shue, J.-H., Suvorova, A. V., & Sibeck, D. G. (2010). Thin magnetosheath as a consequence of the magnetopause deformation: THEMIS observations. *Journal of Geophysical Research (Space Physics)*, *115*, 10203. Retrieved from `http://adsabs.harvard.edu/abs/2010JGRA..11510203J`

Johnson, J. R., Wing, S., & Delamere, P. A. (2014). Kelvin helmholtz instability in planetary magnetospheres. *Space Science Reviews*, *184*(1-4), 1–31.

Karimabadi, H., Krauss-Varban, D., Huba, J., & Vu, H. (2004). On magnetic reconnection regimes and associated three-dimensional asymmetries: Hybrid, hall-less hybrid, and hall-mhd simulations. *Journal of Geophysical Research: Space Physics*, *109*(A9).

Karimabadi, H., Roytershteyn, V., Vu, H. X., Omelchenko, Y. A., Scudder, J., Daughton, W., … Geveci, B. (2014). The link between shocks, turbulence, and magnetic reconnection in collisionless plasmas. *Physics of Plasmas*, *21*, 062308. doi: 10.1063/1.4882875

Lavraud, B., Borovsky, J. E., Génot, V., Schwartz, S. J., Birn, J., Fazakerley, A. N., … Wild, J. A. (2009). Tracing solar wind plasma entry into the magnetosphere using ion-to-electron temperature ratio. *Geophys. Res. Lett.*, *36*, 18109. Retrieved from `http://adsabs.harvard.edu/abs/2009GeoRL..3618109L`

Le Contel, O., Retinò, A., Breuillard, H., Mirioni, L., Robert, P., Chasapis, A., … Saito, Y. (2016, June). Whistler mode waves and Hall fields detected by MMS during a dayside magnetopause crossing. *Geophysical Research Letters*, *43*(12), 5943-5952. doi: 10.1002/2016GL068968

Lindman, E. (1975). "Free-space" boundary conditions for the time dependent wave equation. *J. Comput. Phys.*, *18*(1), 66–78.

Liu, Y.-H., Li, T., Hesse, M., Sun, W., Liu, J., Burch, J., … Huang, K. (2019). Three-dimensional magnetic reconnection with a spatially confined x-line extent: Implications for dipolarizing flux bundles and the dawn-dusk asymmetry. *Journal of Geophysical Research: Space Physics*, *124*(4), 2819–2830.

Lu, J., Wang, M., Kabin, K., Zhao, J., Liu, Z.-Q., Zhao, M., & Li, G. (2015). Pressure balance across the magnetopause: Global mhd results. *Planetary and Space Science*, *106*, 108–115.

Lu, S., Lin, Y., Angelopoulos, V., Artemyev, A., Pritchett, P., Lu, Q., & Wang, X. (2016). Hall effect control of magnetotail dawn-dusk asymmetry: A three-dimensional global hybrid simulation. *Journal of Geophysical Research: Space Physics*, *121*(12), 11–882.

Luo, H., Chen, G., Du, A., & Xu, W. (2013). Solar wind dependence of energy coupling between solar wind and magnetosphere during intense northward imfs. *Planetary and Space Science*, *79*, 82–89.

Masters, A., Slavin, J., DiBraccio, G., Sundberg, T., Winslow, R., Johnson, C., … Korth, H. (2013). A comparison of magnetic overshoots at the bow shocks of mercury and saturn. *Journal of Geophysical Research: Space Physics*, *118*(7), 4381–4390.

Merka, J., Szabo, A., Šafránková, J., & Němeček, Z. (2003). Earth's bow shock and magnetopause in the case of a field-aligned upstream flow: Observation and model comparison. *Journal of Geophysical Research: Space Physics (1978–2012)*, *108*(A7), –.

Němeček, Z., Šafránková, J., Zastenker, G. N., Pišoft, P., & Jelínek, K. (2002, April). Low-frequency variations of the ion flux in the magnetosheath. *Planetary and Space Science*, *50*(5-6), 567-575. doi: 10.1016/S0032-0633(02)00036-3

Omidi, N., Blanco-Cano, X., Russell, C. T., & Karimabadi, H. (2004, January). Dipolar magnetospheres and their characterization as a function of magnetic moment. *Advances in Space Research*, *33*, 1996–2003. doi: 10.1016/j.asr.2003.08.041

Palmroth, M., Ganse, U., Pfau-Kempf, Y., Battarbee, M., Turc, L., Brito, T., … von Alfthan, S. (2018, August). Vlasov methods in space physics and astrophysics. *Living Reviews in Computational Astrophysics*, *4*(1), 1. doi: 10.1007/s41115-018-0003-2

Paral, J., & Rankin, R. (2013). Dawn–dusk asymmetry in the kelvin–helmholtz instability at mercury. *Nature Communications*, *4*(1), 1–5.

Park, J.-S., Shue, J.-H., Kim, K.-H., Pi, G., Němeček, Z., & Å afránková, J. (2016, July). Global expansion of the dayside magnetopause for long-duration radial IMF events: Statistical study on GOES observations. *Journal of Geophysical Research (Space Physics)*, *121*(7), 6480–6492. doi: 10.1002/2016JA022772

Parks, G. K. (1991). Physics of space plasmas-an introduction. *Redwood City, CA, Addison-Wesley Publishing Co., 1991, 547 p.*.

Paschmann, G., Baumjohann, W., Sckopke, N., Phan, T. D., & Luehr, H. (1993, August). Structure of the dayside magnetopause for low magnetic shear. *Journal of Geophysica Research(Space Physics)*, *98*(A8), 13409-13422. doi: 10.1029/93JA00646

Paularena, K., Richardson, J., Kolpak, M., Jackson, C., & Siscoe, G. (2001). A dawn-dusk density asymmetry in earth's magnetosheath. *Journal of Geophysical Research: Space Physics*, *106*(A11), 25377–25394.

Phan, T. D., Paschmann, G., Baumjohann, W., Sckopke, N., & Luehr, H. (1994, January). The magnetosheath region adjacent to the dayside magnetopause: AMPTE/IRM observations. *Journal of Geophysical Research (Space Physics)*, *99*(A1), 121-142. doi: 10.1029/93JA02444

Pi, G., Němeček, Z., Šafránková, J., Grygorov, K., & Shue, J.-H. (2018). Formation of the dayside magnetopause and its boundary layers under the radial imf. *Journal of Geophysical Research: Space Physics*, *123*(5), 3533–3547.

Samsonov, A. (2006, January). Numerical modelling of the Earth's magnetosheath for different IMF orientations. *Advances in Space Research*, *38*(8), 1652-1656. doi: 10 .1016/j.asr.2005.06.009

Samsonov, A. A. (2011, January). Propagation of inclined interplanetary shock through the magnetosheath. *Journal of Atmospheric and Solar-Terrestrial Physics*, *73*, 30–39. doi: 10.1016/j.jastp.2009.10.014

Samsonov, A. A., Bogdanova, Y. V., Branduardi-Raymont, G., Sibeck, D. G., & Toth, G. (2020). Is the Relation Between the Solar Wind Dynamic Pressure and the Magnetopause Standoff Distance so Straightforward? *Geophys. Res. Lett.*, *47*(8). doi: 10.1029/2019GL086474

Samsonov, A. A., Němeček, Z., Šafránková, J., & Jelínek, K. (2012, May). Why does the subsolar magnetopause move sunward for radial interplanetary magnetic field? *Journal of Geophysical Research (Space Physics)*, *117*, 5221. doi: 10.1029/2011JA017429

Samsonov, A. A., Sibeck, D. G., Å afránková, J., Němeček, Z., & Shue, J. H. (2017, March). A method to predict magnetopause expansion in radial IMF events by MHD simulations. *Journal of Geophysical Research (Space Physics)*, *122*(3), 3110-3126. doi: 10.1002/2016JA023301

Shue, J. H., Chao, J. K., Fu, H. C., Russell, C. T., Song, P., Khurana, K. K., & Singer,

H. J. (1997, May). A new functional form to study the solar wind control of the magnetopause size and shape. *Journal of Geophysical Research (Space Physics)*, *102*(A5), 9497-9512. doi: 10.1029/97JA00196

Shue, J.-H., Chao, J.-K., Song, P., McFadden, J., Suvorova, A., Angelopoulos, V., … Plaschke, F. (2009). Anomalous magnetosheath flows and distorted subsolar magnetopause for radial interplanetary magnetic fields. *Geophysical Research Letters*, *36*(18).

Sibeck, D. G., Allen, R., Aryan, H., Bodewits, D., Brandt, P., Branduardi-Raymont, G., … others (2018). Imaging plasma density structures in the soft x-rays generated by solar wind charge exchange with neutrals. *Space Science Reviews*, *214*(4), 79.

Sibeck, D. G., Decker, R. B., Mitchell, D. G., Lazarus, A. J., Lepping, R. P., & Szabo, A. (2001). Solar wind preconditioning in the flank foreshock: IMP 8 observations. *J. Geophys. Res.*, *106*, 21675–21688. Retrieved from `http://adsabs.harvard.edu/abs/2001JGR...10621675S`

Sorathia, K., Merkin, V., Ukhorskiy, A., Allen, R., Nykyri, K., & Wing, S. (2019). Solar wind ion entry into the magnetosphere during northward imf. *Journal of Geophysical Research: Space Physics*, *124*(7), 5461–5481.

Spreiter, J. R., & Alksne, A. Y. (1969). Plasma flow around the magnetosphere. *Reviews of Geophysics*, *7*(1-2), 11–50.

Suvorova, A., & Dmitriev, A. (2015). Magnetopause inflation under radial imf: Comparison of models. *Earth and Space Science*, *2*(4), 107–114.

Suvorova, A. V., Shue, J. H., Dmitriev, A. V., Sibeck, D. G., McFadden, J. P., Hasegawa, H., … Němeček, Z. (2010, October). Magnetopause expansions for quasi-radial interplanetary magnetic field: THEMIS and Geotail observations. *Journal of Geophysical Research (Space Physics)*, *115*(A10), A10216. doi: 10.1029/2010JA015404

Tan, B., Lin, Y., Perez, J., & Wang, X. (2011). Global-scale hybrid simulation of dayside magnetic reconnection under southward imf: Structure and evolution of reconnection. *Journal of Geophysical Research: Space Physics*, *116*(A2).

Treumann, R. A., & Baumjohann, W. (2013, December). Collisionless Magnetic Reconnection in Space Plasmas. , *1*, 31. (arXiv: 1401.5995) doi: 10.3389/fphy.2013.00031

Turc, L., Tarvus, V., Dimmock, A., Battarbee, M., Ganse, U., Johlander, A., … Palmroth, M. (2020). Asymmetries in the earth's dayside magnetosheath: results from global hybrid-vlasov simulations. *Annales Geophysicae Discussions*, *2020*, 1–24. Retrieved from `https://www.ann-geophys-discuss.net/angeo-2020-13/` doi: 10.5194/angeo-2020-13

Turner, D., Wilson, L., Liu, T., Cohen, I., Schwartz, S., Osmane, A., … others (2018). Autogenous and efficient acceleration of energetic ions upstream of earth's bow shock. *Nature*, *561*(7722), 206–210.

Villasenor, J., & Buneman, O. (1992). Rigorous charge conservation for local electromagnetic field solvers. *Comput. Phys. Commun.*, *69*(2), 306–316.

Šafránková, J., Němeček, Z., Santolík, O., Sibeck, D. G., Zastenker, G. N., & Skalsky, A. (2000). The Flank Magnetopause: Interball Observations. *Advances in Space Research*, *25*, 1503–1510. Retrieved from `http://adsabs.harvard.edu/abs/2000AdSpR..25.1503S`

Walsh, A. P., Haaland, S., Forsyth, C., Keesee, A. M., Kissinger, J., Li, K., … Taylor, M. G. G. T. (2014, July). Dawn-dusk asymmetries in the coupled solar wind-magnetosphere-ionosphere system: a review. *Annales Geophysicae*, *32*, 705–737. Retrieved from `https://ui.adsabs.harvard.edu/abs/2014AnGeo..32..705W` doi: 10.5194/angeo-32-705-2014

Walsh, B. M. (2017). Magnetopause plasma parameters and asymmetries in solar wind–magnetosphere coupling. *Dawn-Dusk Asymmetries in Planetary Plasma Environments*, 29–39.

Walsh, B. M., Sibeck, D. G., Wang, Y., & Fairfield, D. H. (2012). Dawn-dusk asymmetries in the Earth's magnetosheath. *Journal of Geophysical Research (Space Physics)*, *117*, 12211. Retrieved from `http://adsabs.harvard.edu/abs/2012JGRA..11712211W`

Wang, C.-P., Gkioulidou, M., Lyons, L. R., & Angelopoulos, V. (2012). Spatial distributions of the ion to electron temperature ratio in the magnetosheath and plasma sheet. *Journal of Geophysical Research: Space Physics*, *117*(A8).

Wang, C.-P., Lyons, L. R., Weygand, J. M., Nagai, T., & McEntire, R. W. (2006). Equatorial distributions of the plasma sheet ions, their electric and magnetic drifts, and magnetic fields under different interplanetary magnetic field bz conditions. *Journal of Geophysical Research: Space Physics*, *111*(A4).

Wang, J., Guo, Z., Ge, Y. S., Du, A., Huang, C., & Qin, P. (2018, October). The responses of the earth's magnetopause and bow shock to the IMF B_z and the solar wind dynamic pressure: a parametric study using the AMR-CESE-MHD model. *Journal of Space Weather and Space Climate*, *8*, A41. doi: 10.1051/swsc/2018030

Willis, D. (1978). The magnetopause: Microstructure and interaction with magnetospheric plasma. *Journal of Atmospheric and Terrestrial Physics*, *40*(3), 301–322.

Wing, S., Johnson, J. R., Chaston, C. C., Echim, M., Escoubet, C. P., Lavraud, B., … Wang, C. P. (2014, November). Review of Solar Wind Entry into and Transport Within the Plasma Sheet. *Space Science Reviews*, *184*(1-4), 33-86. doi: 10.1007/s11214-014-0108-9

Yu, Y., & Ridley, A. J. (2009, December). The response of the magnetosphere-ionosphere system to a sudden dynamic pressure enhancement under southward IMF conditions. *Annales Geophysicae*, *27*(12), 4391-4407. doi: 10.5194/angeo-27-4391-2009

Zhang, H., Fu, S., Pu, Z., Lu, J., Zhong, J., Zhu, C., … Liu, L. (2019, aug). Statistics on the magnetosheath properties related to magnetopause magnetic reconnection. *The Astrophysical Journal*, *880*(2), 122. Retrieved from `https://doi.org/10.3847%2F1538-4357%2Fab290e` doi: 10.3847/1538-4357/ab290e

1047 # 6 Figures

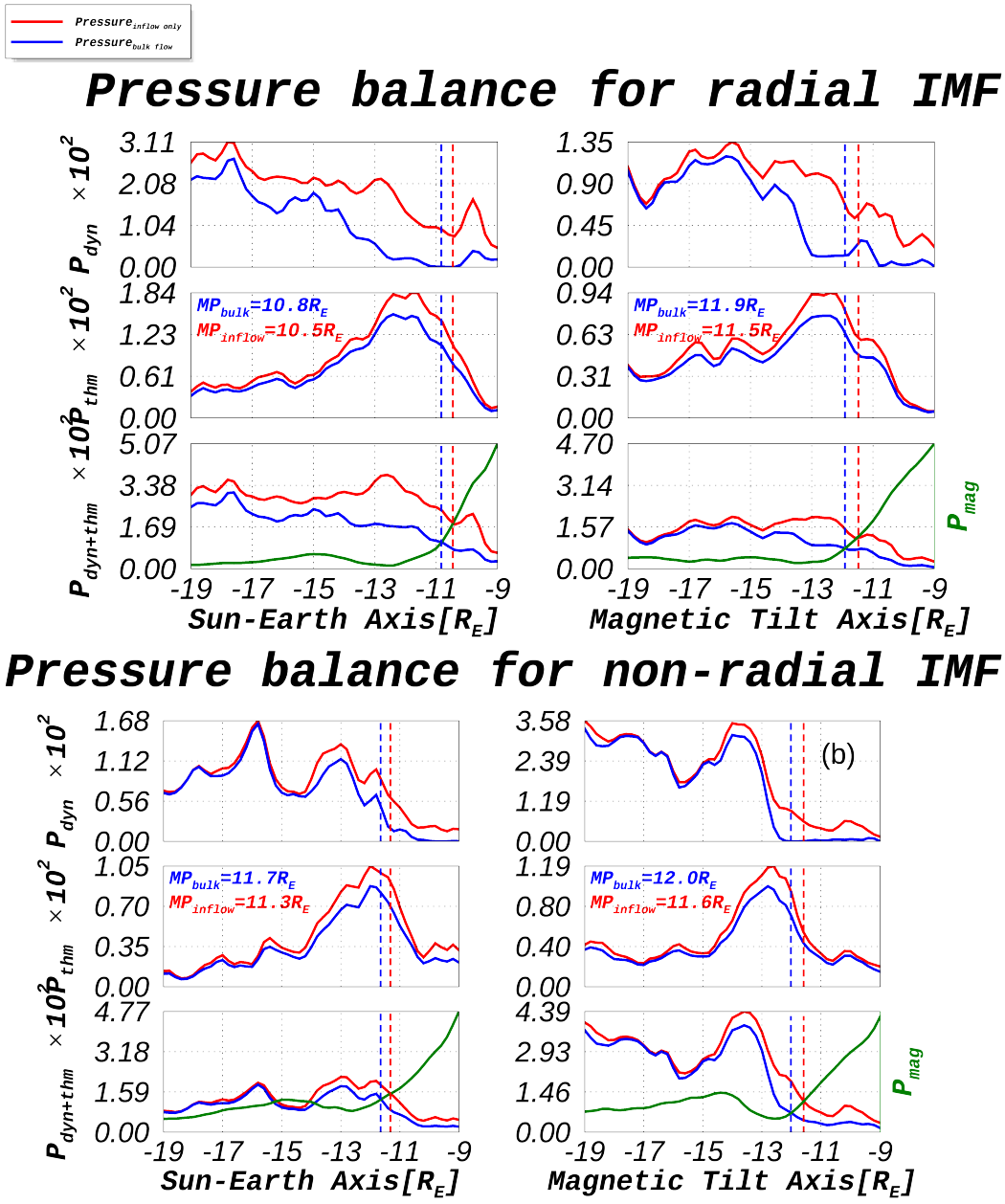

Figure 2. MP size derivation from pressure balance system measured radially at two locations. The MP is derived along the Earth-Sun axis(OX) and along magnetic equator axis (Tilt). Bulk flow(blue) and diffuse population(red) are shown for two IMF orientations(upper for radial and lower for non-radial). The backstreaming ions are not only seen at the bow shock, but everywhere in the simulation box

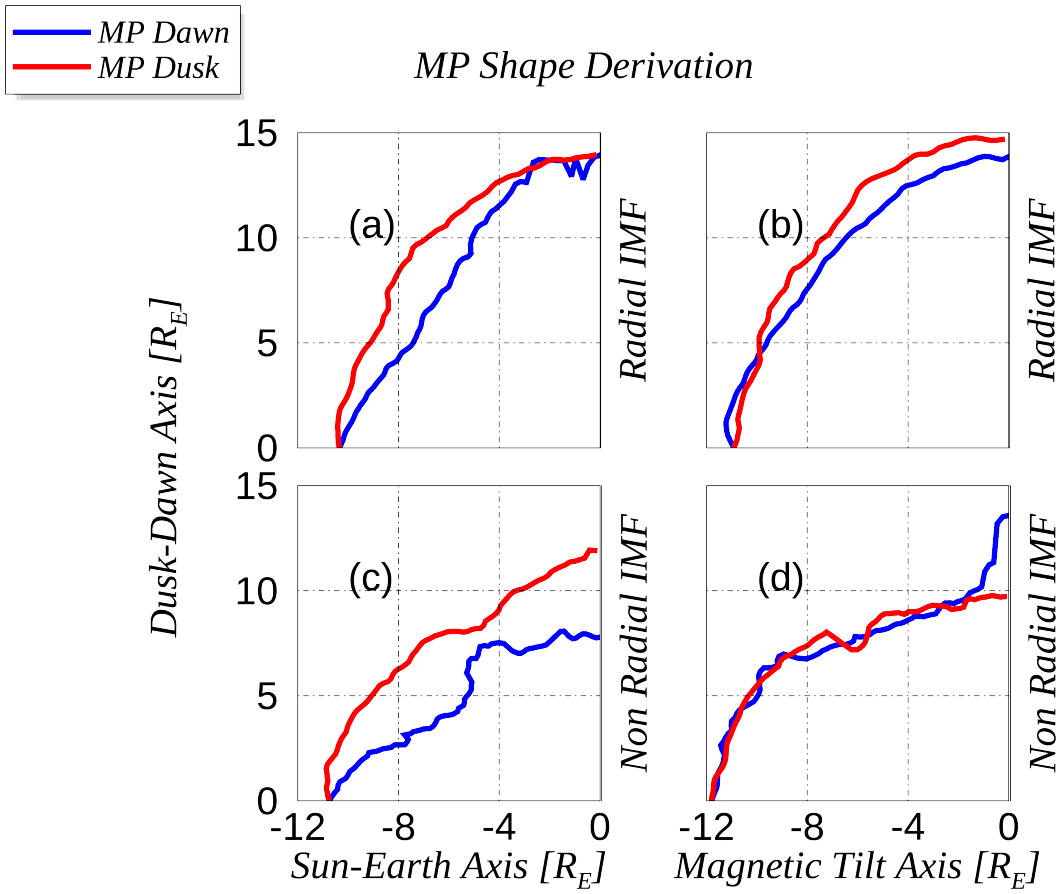

Figure 3. Panels (a) and (b) is the MP shape for radial IMF along Sun-Earth and Magnetic Tilted Axis, similarly panels (c) and (d) are the same for non-radial IMF. This Figure is aimed to show the shape of the MP, though the size shown here is approximately equivalent to the MP sizes derived from the density steepening.

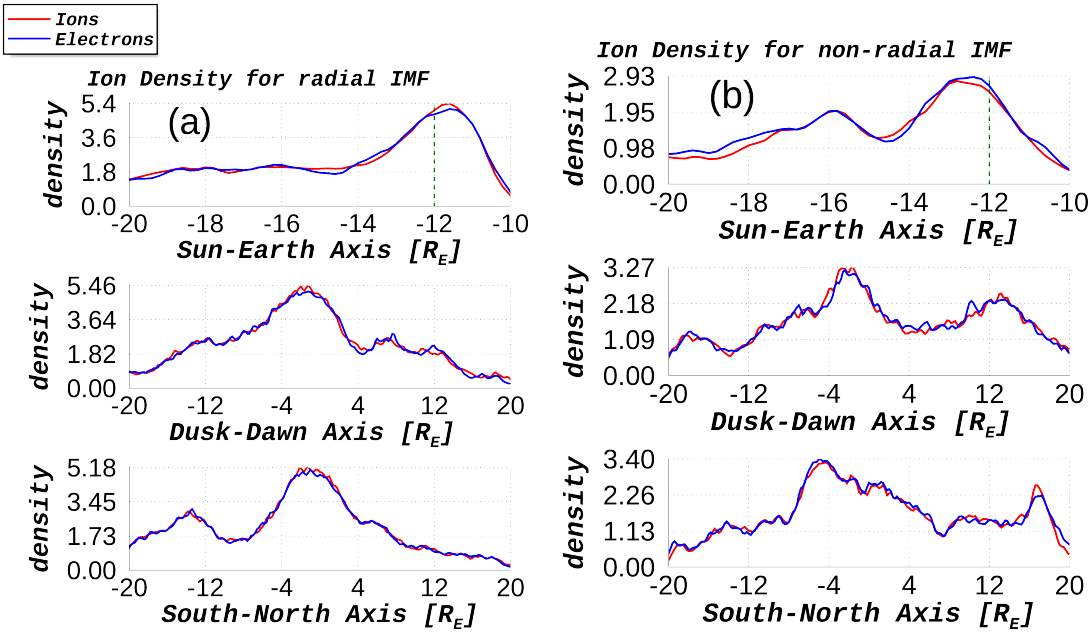

Figure 4. Ion and electron densities are plotted in 3D, along OX(Y=Z=0), OY(X=12, and Z=0), and OZ(X=12, and Y=0)), just outside the MP for radial IMF in panel A and for non-radial IMF in panel B. Their values are normalized to the initial densities. The density profile is plotted only in the dayside magnetosphere. This figure also shows the plasma quasi neutrality.

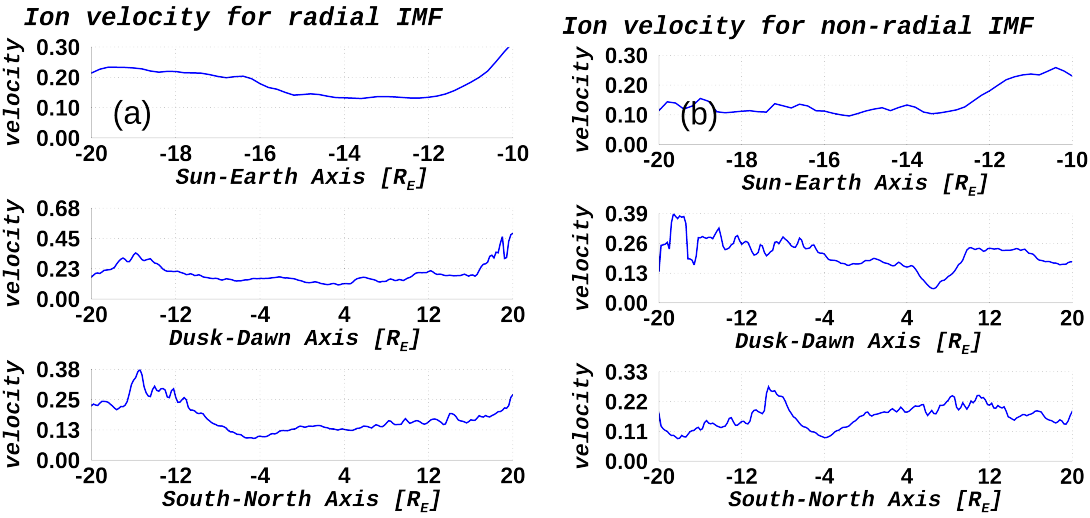

Figure 5. Ion velocity modulus for both IMF orientation are plotted in 3D as in Fig. 4.

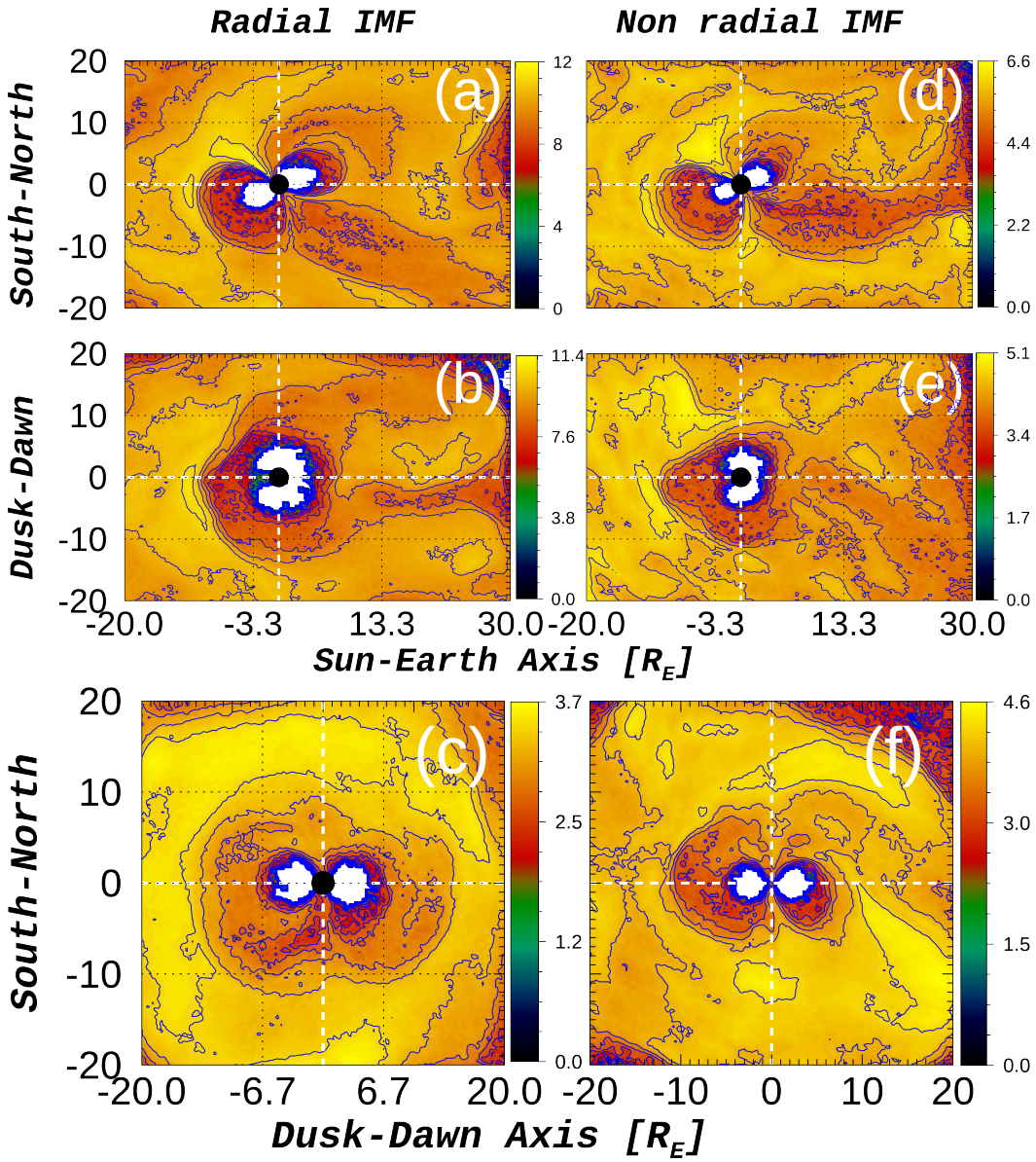

Figure 6. Fields topology in 3D for both IMF orientations. XZ and XY planes are taken in the dayside magnetosphere. YZ plane is plotted at around $12R_E$ outside the MP. Panels (a), (b), and (c) are for radial IMF and panels (d), (e), and (f) are for non radial IMF

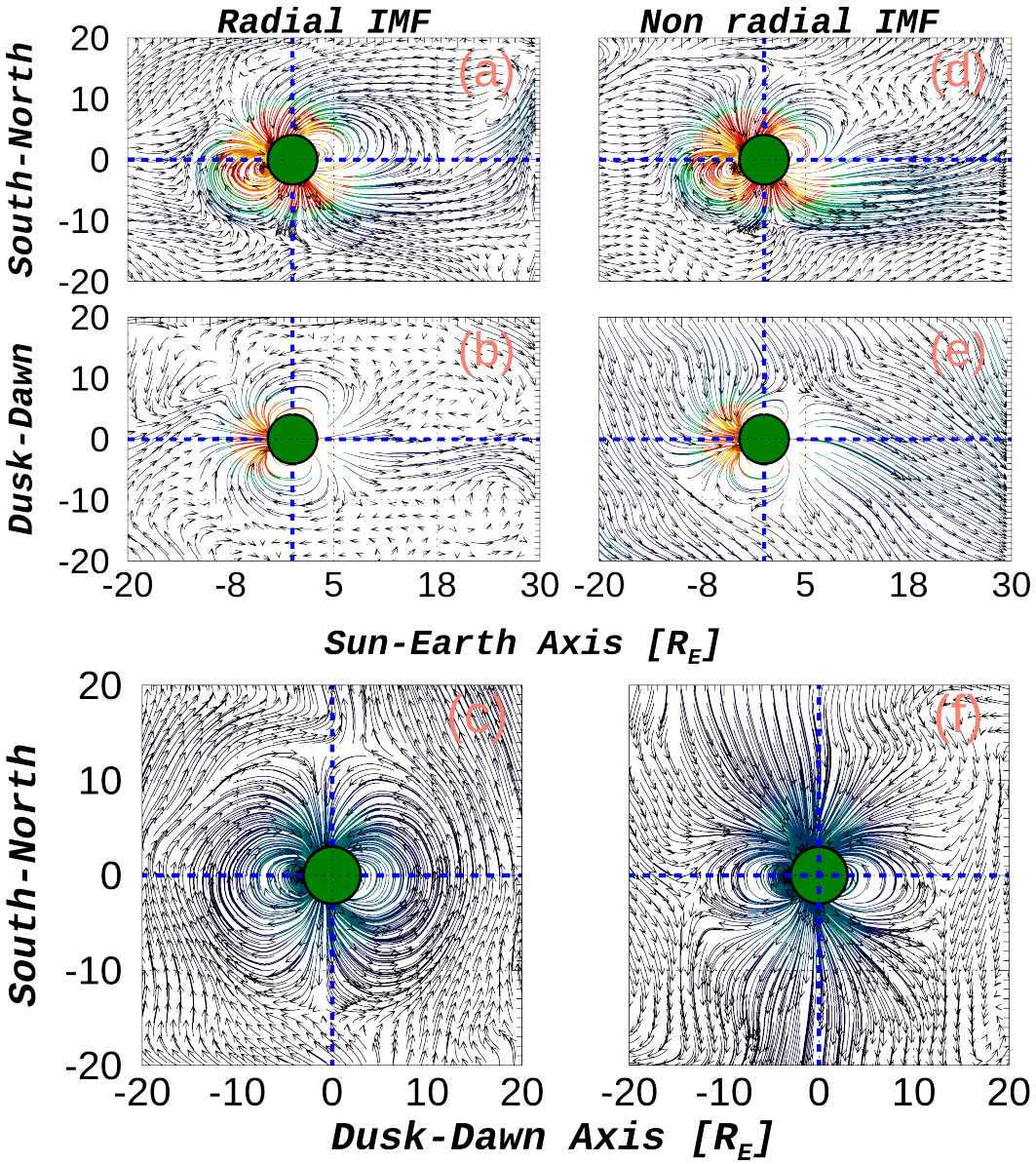

Figure 7. Solar wind density contour in 3D for both IMF orientations. XZ and XY planes are taken in the dayside magnetosphere. YZ contour is plotted at around $12R_E$ outside the MP. Panels (a), (b), and (c) are for radial IMF and panels (d), (e), and (f) are for non radial IMF

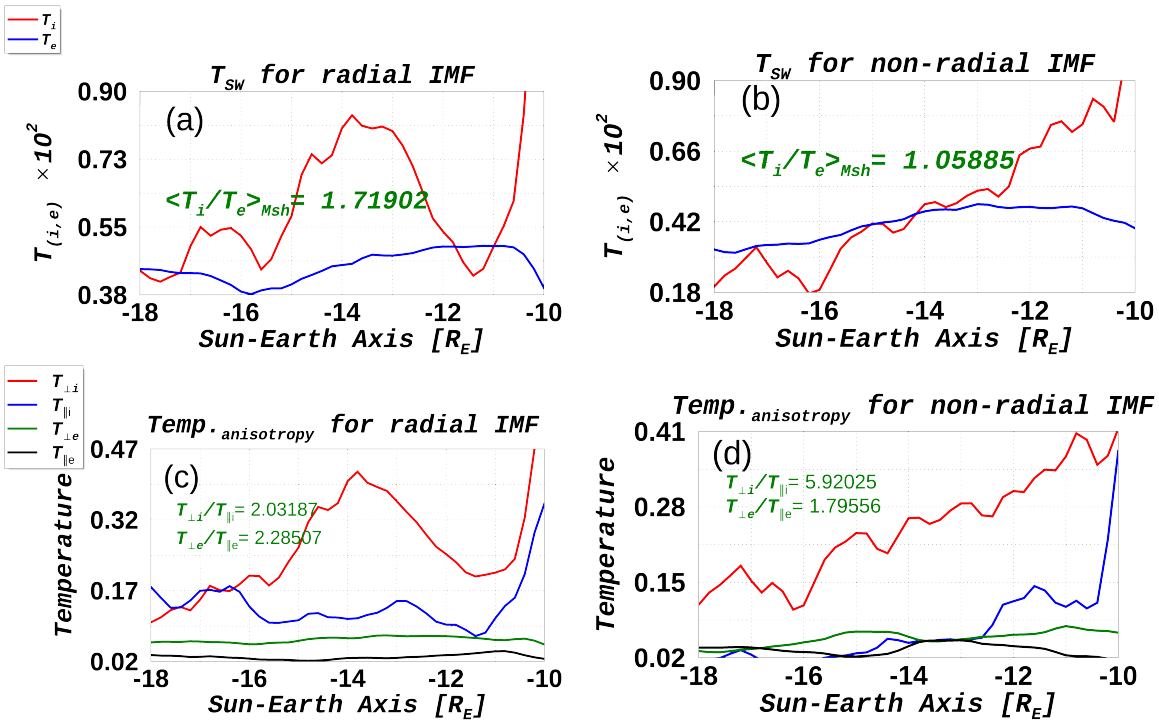

Figure 8. Ion and electron temperatures for both IMF orientations shown in panels (a), and (b). In panel (c) and ((d) temperature anisotropy for ions and electrons are shown. The T_i/T_e ratio is calculated in the magnetosheath in (a) and (b). The plots are taken from -18 to -10 R_E in the dayside magnetosphere.

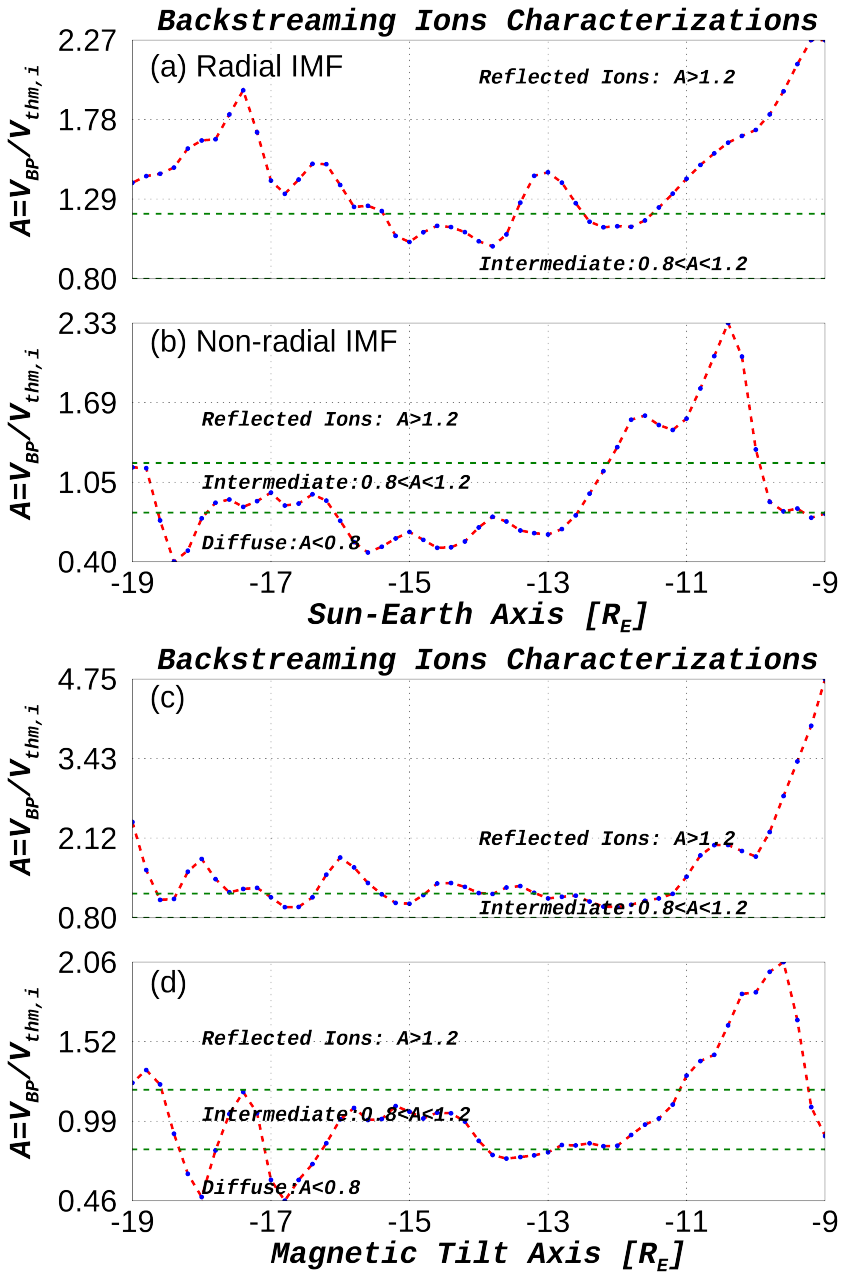

Figure 9. The characterization of backstreaming ions in the dayside magnetosphere based on their bulk flow ratio on thermal speed. Adopted from (Bonifazi & Moreno, 1981b). panel, a and b are taken along OX-axis in XZ plane and panels c, and d are taken along magnetic equator tilt for both IMF orientation. This figure shows the percentage of reflected and diffuse ions of the backstreaming ions.

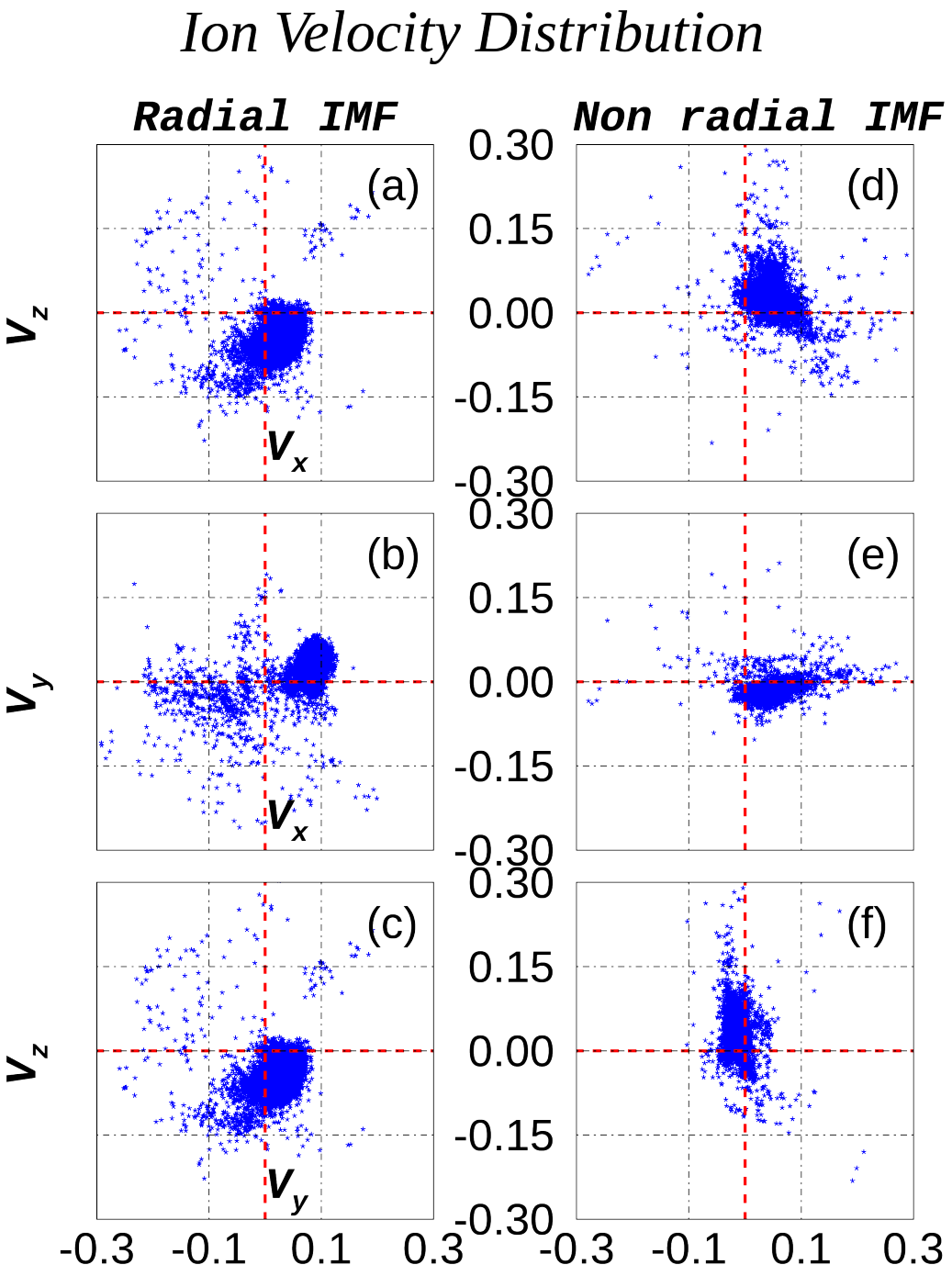

Figure 10. Ion Velocity distribution in the dayside measured from $-20R_E$ to the planet position (z=y=0) along Sun-Earth axis. Left panels are for radial IMF and right panels are for non radial IMF orientation.

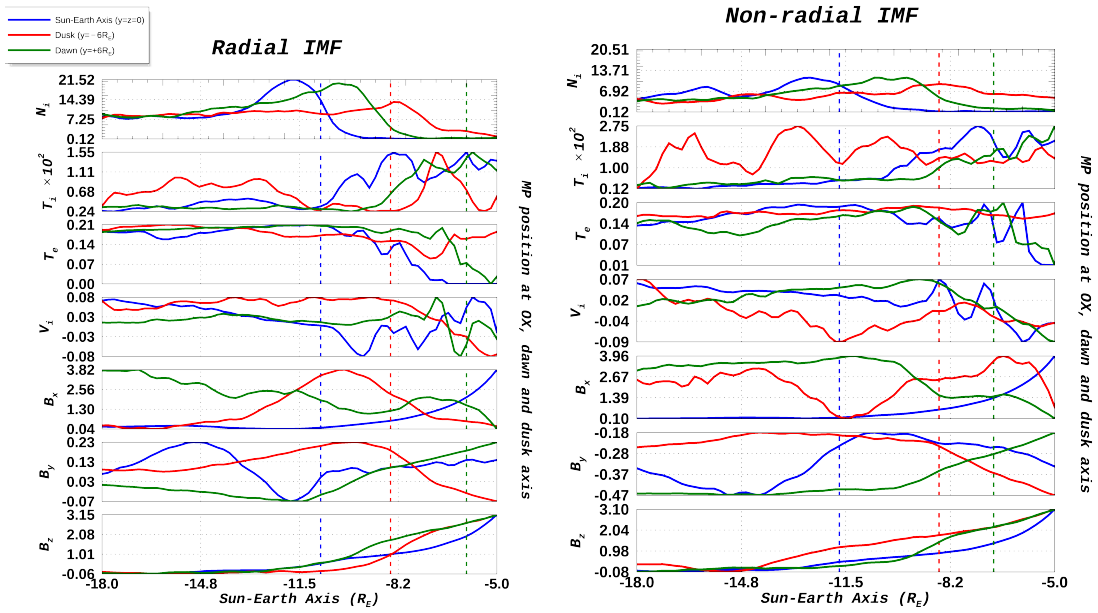

Figure 11. A set of plasma parameters, N_i, T_i, T_e, V_i, B_x, B_y, and B_z are plotted along XZ-plane at three different locations for both IMF orientations. These parameters are plotted along OX-axis and at ±6 on both dusk and dawn directions. Vertical dashed lines show the MP position at the subsolar point(blue), dusk flank(red), and dawn flank(green) quantities show dusk-dawn asymmetry at the $\pm 6 R_E$.